

MIT Open Access Articles

Salient Midlatitude Ionosphere#Thermosphere Disturbances Associated With SAPS During a Minor but Geo#Effective Storm at Deep Solar Minimum

The MIT Faculty has made this article openly available. **Please share** how this access benefits you. Your story matters.

Citation: Aa, E., Zhang, S.-R., Erickson, P. J., Coster, A. J., Goncharenko, L. P., Varney, R. H., & Eastes, R. (2021). Salient midlatitude ionosphere-thermosphere disturbances associated with SAPS during a minor but geo-effective storm at deep solar minimum. *Journal of Geophysical Research: Space Physics*, 126, e2021JA029509.

As Published: <http://dx.doi.org/10.1029/2021ja029509>

Publisher: American Geophysical Union (AGU)

Persistent URL: <https://hdl.handle.net/1721.1/140381>

Version: Author's final manuscript: final author's manuscript post peer review, without publisher's formatting or copy editing

Terms of use: Creative Commons Attribution-Noncommercial-Share Alike



Salient midlatitude ionosphere-thermosphere disturbances associated with SAPS during a minor but geo-effective storm at deep solar minimum

Ercha Aa¹, Shun-Rong Zhang¹, Philip J. Erickson¹, Anthea J. Coster¹, Larisa P. Goncharenko¹, Roger H. Varney², and Richard Eastes³

¹Haystack Observatory, Massachusetts Institute of Technology, Westford, MA, USA.

²Center for Geospace Studies, SRI International, Menlo Park, CA, USA

³Laboratory for Atmospheric and Space Physics, University of Colorado Boulder, Boulder, CO, USA

Key Points:

- A minor but geo-effective storm at deep solar minimum produced intense SAPS, considerable SED structure, and subauroral large-scale TIDs
- Strong westward wind enhancement of 230 m/s and large poleward wind surge of 85 m/s occurred in the post-SAPS interval
- Midlatitude TEC and O/N₂ simultaneously showed large storm-time dynamic features, with a prolonged enhancement followed by a large reduction

Corresponding author: E. Aa, aercha@mit.edu

This is the author manuscript accepted for publication and has undergone full peer review but has not been through the copyediting, typesetting, pagination and proofreading process, which may lead to differences between this version and the [Version of Record](#). Please cite this article as [doi: 10.1029/2021JA029509](https://doi.org/10.1029/2021JA029509).

This article is protected by copyright. All rights reserved.

Abstract

This work conducts a focused study of subauroral ion-neutral coupling processes and mid-latitude ionospheric/thermospheric responses in North America during a minor but quite geo-effective storm on 27–28 September 2019 under deep solar minimum conditions. Several prominent storm-time disturbances and associated electrodynamic/dynamics were identified and comprehensively analyzed using Millstone Hill and Poker Flat incoherent scatter radar measurements, Fabry-Perot interferometer data, total electron content (TEC) data from Global Navigation Satellite System observations, and thermospheric composition O/N₂ data from the Global-scale Observations of Limb and Disk (GOLD) mission. Despite solar minimum conditions, this minor storm produced several prominent dynamic features, in particular (1) Intense subauroral polarization stream (SAPS) of 1000 m/s, overlapping with a deepened main trough structure. (2) An enhanced westward wind of 230 m/s and a significant poleward wind surge of 85 m/s occurred in the post-SAPS period. (3) Large-scale traveling ionospheric disturbances (TIDs) were generated and propagated equatorward across mid-latitudes in the storm main phase. TID characteristics were significantly affected by SAPS, evolving into divergent propagation patterns. (4) SAPS was situated on the poleward edge of a considerable storm-enhanced density structure. (5) The midlatitude ionosphere and thermosphere exhibited a prolonged positive storm effect in the main phase and beginning of recovery phase, with 5–10 TECU increase and 10–30% O/N₂ enhancement for 12 hours. This was followed by a considerable negative storm effect with 5–10 TECU and 20–40% O/N₂ decrease. Results show that minor storm intervals can produce substantial mid-latitude ionospheric and thermospheric dynamics in low solar flux conditions.

1 Introduction

During a geomagnetic storm, intense injection of solar wind-magnetospheric energy and momentum into the coupled ionosphere-thermosphere (I-T) system occurs through enhanced electric fields, currents, and particle precipitation. These enhanced inputs are known to cause significant perturbations in the coupled I-T system (Buonsanto, 1999). In particular, dramatic and complicated local/global changes may occur in the I-T system in response to various chemical, dynamic, and electrodynamic driving processes, such as Joule heating, ion-drag forcing, penetration electric field, etc. (Mendillo, 2006; Richmond & Lu, 2000). Moreover, besides the traditional concentration in storm effects within auroral/polar and equatorial regions, the midlatitude and subauroral ionosphere also experiences substantial dynamic structuring and increase in variability. These mid-latitude I-T effects have been the subject of many recent community studies especially in the past decade, as the observed response can exhibit far more storm-time dynamics than would be otherwise anticipated (e.g., Ferdousi et al., 2019; Raeder et al., 2016; Zhang et al., 2015). Furthermore, steep electron density gradients therein can pose detrimental effects on modern navigation and communication systems (e.g., Coster & Foster, 2007; Doherty et al., 2004). For these reasons, characterizing the storm-time mid-latitude ionosphere and thermosphere perturbations and understanding the intrinsic mechanisms in triggering those perturbations are of considerable importance in frontier space weather research.

Generally, midlatitude ionosphere-thermosphere responses to a geomagnetic storm are primarily determined by various ion-neutral coupling mechanisms and relevant electrodynamic processes. These include (1) Momentum transfer via ion drag: Strong ion convection in the storm-time auroral/subauroral region can act as a driver to accelerate neutrals, resulting in large modifications to the horizontal thermospheric neutral wind pattern (Killeen & Roble, 1984; Rishbeth, 1979). Conversely, the neutral circulation that is set up by the above-mentioned ion drag can also influence the ionosphere to drive Hall and field-aligned currents when the magnetospheric electric field is suddenly inhibited, in a configuration known as the “flywheel” effect (Deng et al., 1993; Lyons et al., 1985).

68 (2) Energy transfer via heating: Electromagnetic energy from the magnetosphere can
69 be transferred to the ionospheric plasma and further dissipate into the thermosphere via
70 ion-neutral coupling in the form of Joule heating. This process further modifies the global
71 neutral circulation as well as thermospheric composition (Schunk & Nagy, 2000). More-
72 over, at subauroral latitudes, the subauroral polarization stream (SAPS, Foster and Burke
73 (2002)) will cause enhanced ion-neutral frictional heating and lead to considerable ion
74 upflow associated with thermal expansion (Yeh & Foster, 1990; Erickson et al., 2010; Zhang,
75 Erickson, et al., 2017). (3) Neutral dynamics and composition effects: Pressure gradi-
76 ents due to the intense Joule and particle heating in the high-latitude ionosphere will
77 cause atmospheric upwelling and equatorward neutral wind surge, leading to both iono-
78 spheric disturbance dynamo (Blanc & Richmond, 1980) and possible thermospheric com-
79 position (e.g., O/N₂) changes (Fuller-Rowell et al., 1994). The direct effects of neutral
80 wind through ion transport along field lines, as well as indirect effects through compo-
81 sition variation and the generation of dynamo electric fields, significantly impact the iono-
82 sphere. These underlying processes generate significant regional/global increases (pos-
83 itive storm) or decreases (negative storm) in TEC and electron density (e.g., Lu et al.,
84 2014). (4) Prompt penetration electric field (PPEF) and disturbance dynamo electric
85 field (DDEF): In response to storm-induced variations in the solar wind-magnetosphere
86 dynamo, there is a time-delayed development of the Region-2 field-aligned current sys-
87 tem with respect to the Region-1 field-aligned current. This delay leads to the build-up
88 of an undershielding (overshielding) PPEF during suddenly enhanced (decreased) mag-
89 netospheric convection electric field conditions (Huang et al., 2010; Kikuchi et al., 1978;
90 Klimenko & Klimenko, 2012; Lu et al., 2012). For the DDEF, the above-mentioned equa-
91 torward neutral wind surge can subsequently drive a westward wind component due to
92 the Coriolis force, generating a disturbed zonal electric field in the mid- and low-latitude
93 ionosphere via dynamo process (Blanc & Richmond, 1980; Maruyama et al., 2005). When
94 all these factors are combined, the combination of electric fields, neutral winds, and ther-
95 mospheric composition changes will generate complicated ionospheric and thermospheric
96 variations during a storm.

97 In parallel with studies of these dynamic effects, continued community interest over
98 the last several decades has focused on specifying the mechanisms and drivers behind
99 storm-time midlatitude ionosphere and thermosphere dynamic features. Prominent drivers
100 and associated characteristics are still a matter of study but include: (1) The subaural
101 polarization stream (SAPS, Foster and Burke (2002)), which refers to intense west-
102 ward plasma flows (a few hundred m/s) driven by large poleward electric fields in the
103 subauroral ionosphere equatorward of the auroral precipitation zone (Erickson et al., 2011;
104 Foster & Vo, 2002). SAPS is a broad term that can under certain circumstances be as-
105 sociated with embedded phenomena, such as latitudinally narrow and intense flow chan-
106 nel known as subauroral ion drifts (SAID) (Anderson et al., 1991; Spiro et al., 1979), or
107 polarization jets (Galperin et al., 1974). (2) Storm-enhanced density (SED, Foster (1993)),
108 which describes a significant storm-time electron density or total electron content (TEC)
109 enhancement in the local afternoon ionosphere at mid- and subauroral latitudes (Mendillo,
110 2006). SED structures sometimes extend to higher latitudes along a sunward/poleward
111 elongated ridge and form a plume, which can occasionally convect into the cusp region
112 and then into the polar cap (Foster et al., 2005). (3) Storm-induced traveling ionospheric/atmospheric
113 disturbances (TIDs/TADs). Storm-time energy deposition in the auroral and subaural
114 regions can generate large amplitude atmospheric gravity waves (AGWs), which man-
115 ifest in the ionosphere as large-scale TIDs (Hunsucker, 1982). These underlying processes
116 are of great importance in transporting high-latitude energy and momentum deposition
117 into higher altitudes and lower latitudes (Richmond, 1978). (4) Negative and positive
118 ionospheric storm effects, with main drivers being electric fields, thermospheric neutral
119 winds, and composition changes. As partially described above, a negative ionospheric
120 storm is primarily caused by a decrease in O/N₂ density ratio due to thermospheric com-
121 position changes (Fuller-Rowell et al., 1994). In contrast, explaining the positive iono-
122 spheric storm remains a difficult issue since it involves many complicated and compet-

123 ing drivers, such as penetration electric field (PPEF, Kikuchi et al. (1978)) effects, dis-
124 turbance dynamo electric field (DDEF, Blanc and Richmond (1980)) effects, as well as
125 forcing from equatorward thermospheric neutral winds and TAD/TIDs (Balan et al., 2010).

126 Recently, our understanding of storm-time midlatitude ion-neutral coupling and
127 electrodynamic processes has greatly advanced through community-wide investigation
128 on I-T responses to a few intense geomagnetic storms, especially in the maximum and
129 declining phase of the Solar Cycle 24. These events include but not limited to the St.
130 Patrick's Day storms during 17-18 March 2013 and 2015 (e.g., Astafyeva et al., 2015; Nava
131 et al., 2016; Huang et al., 2016; Huba et al., 2017; Yue et al., 2016; Zakharenkova et al.,
132 2016; Zhong et al., 2016; Zhang, Erickson, et al., 2017; Zhang, Zhang, et al., 2017), 22-
133 23 June 2015 storm (e.g., Astafyeva et al., 2017; Singh & Sripathi, 2017), Memorial Day
134 storm on 27-28 May 2017 (e.g., Jonah et al., 2018; Liu et al., 2019), 07-08 September 2017
135 storm (e.g., Aa et al., 2019; Lei et al., 2018; Jimoh et al., 2019; Zhang et al., 2019), as
136 well as the 25-26 August 2018 storm (Astafyeva et al., 2020). Although significant progress
137 has been made through prior studies on these intense storms, the spatial/temporal evolu-
138 tion of the I-T system in each storm can be quite different and often lacks a unified
139 explanation of the various responses. Moreover, even a seemingly modest storm around
140 a deep solar minimum period can be highly geo-effective in causing severe observed dis-
141 turbances in the I-T system (Watari, 2017). Of these features, midlatitude ion-neutral
142 coupling processes and their physical drivers are still in need of coordinated, multi-sensor
143 studies through observational campaigns for modest storms to allow comparison with
144 responses seen in intense storms near solar maximum. Such studies of modest storm re-
145 sponse provide key information for a more complete understanding of storm-time I-T re-
146 sponse.

147 In this study, we investigate a minor but very geo-effective geomagnetic storm that
148 occurred on 27-28 September 2019 in the deep minimum of solar cycle 24. The regional
149 subauroral/midlatitude ionosphere and thermosphere responses, such as plasma drift,
150 neutral wind, electron density, were measured by a coordinated observational campaign
151 within the North American longitude sector at subauroral latitudes near Millstone Hill
152 (42.8°N , 71.5°W , MLAT: 52°). We comprehensively analyze I-T responses during this
153 period to study several SAPS-related ion-neutral coupling processes. Ionospheric and ther-
154 mospheric direct observations employed in this study include Millstone Hill incoherent
155 scatter radar (MHISR) measurements and Fabry-Perot Interferometer (FPI) measure-
156 ments. In addition, the storm-time total electron content (TEC) from global navigation
157 satellite system (GNSS) measurements and thermospheric O/N_2 density ratio data de-
158 rived from Global-scale Observations of Limb and Disk (GOLD) measurements over the
159 American sector will also be collectively investigated to understand the ionospheric storm
160 effect and its underlying drivers. Moreover, measurements from the high-latitude Poker
161 Flat incoherent scatter radar (PFISR) will also be used to extend and corroborate the
162 above-mentioned results.

163 As a general statement, the appearance of several significant I-T disturbances in
164 a minor storm near the solar minimum is quite unusual. In particular, the 27-28 Septem-
165 ber 2019 storm triggered a series of bright features, including intense SAPS flow, a con-
166 siderable SED, strong zonal and meridional neutral wind perturbation, subauroral TIDs/TADs,
167 and complicated positive and negative storm effects. Despite the relatively minor storm
168 conditions, many of these features became comparable to those reported in earlier stud-
169 ies of severe geospace storms. These features included large SAPS and SED (Foster et
170 al., 2007; Zou et al., 2013), strong neutral wind disturbances in zonal and particularly
171 in meridional components (Zhang et al., 2015), as well as significant TIDs/TADs in the
172 subauroral latitudes (Guo et al., 2018; Zhang et al., 2019). In general, therefore, a straight-
173 forward connection to severe system forcing is not possible for this minor storm, and phys-
174 ical processes responsible for these features thus remain highly debatable. In aggregate,

175 these factors motivated this study as a unique opportunity to advance the current un-
176 derstanding of storm-time electrodynamic and neutral dynamics at mid-latitudes.

177 2 Data and Instrumentation

178 2.1 Millstone Hill incoherent scatter radar

179 The Millstone Hill incoherent scatter radar system uses the Thomson or incoher-
180 ent scatter remote ionospheric sensing technique (Evans, 1969), considered one of the
181 most powerful ground-based methods for ionospheric dynamic observations. Millstone
182 Hill has provided extensive and valuable auroral, subauroral, and mid-latitude observa-
183 tions in the North American sector. (e.g., Buonsanto et al., 1992; Foster et al., 2005).
184 The radar system uses a 2.5-megawatt transmitter in combination with multiple large
185 antennas and highly sensitive radio receivers to measure ionospheric plasma state pa-
186 rameters (e.g., temperature, density, composition, velocity) with full altitude profiles be-
187 tween 100–1000 km. (Foster & Vo, 2002; Erickson et al., 2011). The Millstone Hill in-
188 coherent scatter radar system is equipped with a 46 m diameter full steerable MISA an-
189 tenna and a 68 m diameter fixed zenith antenna. The MISA steerable antenna has an
190 extensive field-of-view which was configured in the observations reported in this study
191 to conduct a wide-range azimuth scan from $+20^\circ$ to -100° at a fixed elevation of $\sim 6^\circ$,
192 spanning over 30° in latitude and more than four hours in local time at F-layer (Aa, Er-
193 ickson, et al., 2020). On a near-simultaneous basis, the system’s zenith antenna provided
194 local altitude profiles in both E and F regions. For more details about Millstone Hill in-
195 coherent scatter radar data processing procedures, readers may refer to Zhang, Erick-
196 son, et al. (2017).

197 2.2 Fabry-Perot Interferometer

198 The ground-based Fabry-Perot interferometer at Millstone Hill measures thermo-
199 spheric horizontal winds at an altitude of ~ 250 km. Observations are based on Doppler
200 shifts in the upper atmosphere 630.0 nm nightglow emission occurring due to dissocia-
201 tive recombination of O_2^+ (Zhang et al., 2015).

202 2.3 GNSS TEC

203 GNSS TEC data are generated at the Massachusetts Institute of Technology’s Haystack
204 Observatory through a processing algorithm employing 6000+ worldwide GNSS receivers.
205 Resulting gridded TEC products are distributed through the Madrigal data system with
206 a spatial resolution of 1° (longitude) \times 1° (latitude) and a temporal cadence of 5 min
207 (Rideout & Coster, 2006; Vierinen et al., 2016). Besides absolute TEC, in this study, we
208 also examined detrended TEC (dTEC) to analyze both large-scale ionospheric variation
209 and wave-like traveling ionospheric disturbances associated with storm-time electrody-
210 namics and dynamics. dTEC is calculated by filtering out the background TEC trend
211 derived from a Savitzky-Golay low-pass filter method, employing a convolution process
212 with the least-square fitting of successive subsets of TEC data points of given window
213 size (30 min in this study) (Savitzky & Golay, 1964; Zhang et al., 2019). A threshold of
214 15° elevation cutoff is implemented to remove satellite-receiver ray paths close to the hori-
215 zon.

216 2.4 GOLD O/N₂ data

217 The GOLD instrument includes two identical far-ultraviolet (FUV) imaging spec-
218 trometers operating at a geostationary orbit over the longitude of 47.5° W. GOLD FUV
219 observations image Earth’s ionosphere and thermosphere by measuring airglow emissions
220 (~ 132 – 162 nm) at different cadences from the daytime disk, limb, occultation, and night-

time disk (Eastes et al., 2019; McClintock et al., 2020). The GOLD measurements are equivalent approximately to a constant pressure surface in the lower thermosphere (Eastes et al., 2020). This study uses the O/N₂ column-integrated density ratio derived from daytime disk imaging of OI 135.6 nm and the N₂ Lyman-Birge-Hopfield (LBH) emission measurement. The O/N₂ ratio is a proxy of thermospheric composition change and a key component in the analysis of storm-time variation in the I-T system.

2.5 The Poker Flat Incoherent Scatter Radar (PFISR)

PFISR is an incoherent scatter radar situated in Alaska at the Poker Flat Research Range (65.13°N, 147.47°W), at a location approximately corresponding to a magnetic L-shell coordinate of ~ 5 . The boresight of the PFISR antenna is tilted to the geomagnetic north with an elevation angle of 74° and a azimuth angle of 15° (Semeter et al., 2009; Varney et al., 2009). PFISR is a phased array radar that can transmit and receive on multiple frequency channels near 450 MHz as well as rapid pulse-to-pulse steering. This allows for almost simultaneous observations in various directions.

2.6 Other observations

Besides the above-mentioned datasets, the Defense Meteorological Satellite Program (DMSP) F18 satellite cross-track plasma drift measurements will also be used. The DMSP F18 satellite flies in a sun-synchronous polar orbit approximately along the dusk-dawn meridian at an altitude of ~ 840 km. Cross-track plasma drift was measured by the Special Sensor-Ions, Electrons, and Scintillation (SSIIES) instrument onboard DMSP. A description of this dataset can be found in Hairston et al. (2016) and references therein.

3 Interplanetary and Geomagnetic conditions of 25-30 September 2019

Figure 1 shows the temporal variation of solar wind proton density, solar wind speed and dynamic pressure, interplanetary magnetic field (IMF) B_y and B_z components, K_p and F10.7 index, interplanetary electric field, as well as the longitudinally symmetric index (SYM-H) from 25 September to 01 October 2019. Solar activity was at a very low level during this period, with F10.7 ranging from 66 to 68 SFU (1 SFU = $10^{-22} \text{W/m}^2/\text{Hz}$). Both solar wind plasma density and dynamic pressure exhibit sudden enhancements during 06–12 UT on 27 September that precede the velocity increase. This is a noticeable signature of stream interactions producing compressed plasma in the leading edge of the stream, due to the influence of a recurrent positive polarity coronal hole high-speed stream. The solar wind speed showed considerable enhancement after 12 UT on 27 September from ~ 350 km/s to ~ 700 km/s. IMF B_z exhibited intermittent fluctuations with two considerable southward excursions on 27 September. Specifically, B_z first became slightly negative at ~ 12 UT and remained southward for about 2–3 hours before temporarily returning to zero. Later, IMF B_z exhibited a moderate southward excursion again, reaching a minimum value of -8.2 nT at 20:00 UT. At the same time as the IMF B_z southward excursion, IMF B_y turned from negative to positive. A modest geomagnetic storm subsequently occurred due to the above-mentioned solar wind and IMF conditions. A sudden storm impulse was registered in the symmetric H-component (SYM-H) index at ~ 6 UT on 27 September, followed by the compression of the magnetosphere that marked the starting of the initial phase at ~ 9 UT. After the beginning of the main phase at $\sim 12:20$ UT, the SYM-H index gradually became more negative during main storm phase, reaching a minimum value of -60 nT at 23:05 UT on 27 September. Also, the K_p index reached 5+ during 18–24 UT on 27 September. Taken as a whole, these parameters would nominally lead to a classification of this disturbance as a minor geomagnetic storm around the deep minimum of solar cycle 24, based on National Oceanic and Atmospheric Administration space weather scales (<https://www.swpc.noaa.gov/noaa-scales-explanation>). This classification implies a corresponding expectation of limited ionosphere and ther-

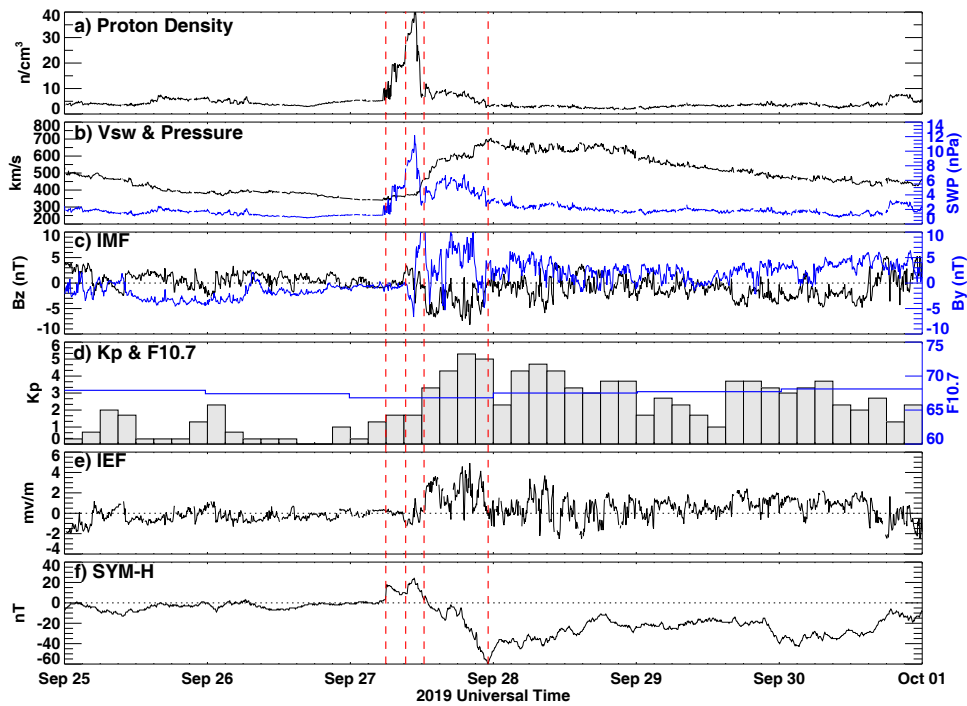


Figure 1. Temporal variation of (a) solar wind proton density, (b) solar wind speed and dynamic pressure, (c) interplanetary magnetic field (IMF) B_y and B_z , (d) Kp and F10.7 index, (e) interplanetary electric field (IEF), and (f) longitudinally symmetric index (SYM-H) during Sep 25–Oct 01, 2019. Four vertical red dashed lines show the starting time of the sudden impulse (~ 6 UT), initial phase (~ 9 UT), main phase (~ 12.3 UT), and recovery phase (~ 23 UT) of the storm occurring on September 27, respectively.

270 mosphere response. However, as will be seen in the following sections, this storm was ac-
 271 tually a highly geo-effective one that triggered a series of noticeable I-T disturbances and
 272 responses, especially in the American sector. The results of this study suggest that Dst
 273 and Kp may not always be sufficient proxies to characterize a storm's I-T effects, and
 274 additional conditions need to be considered.

275 4 Results

276 Results and discussion of storm-time I-T responses during the minor storm event
 277 in this study are elaborated in this section in the following order: (1) SAPS in the North
 278 American sector measured by the Millstone Hill incoherent scatter radar and DMSP satel-
 279 lites. (2) Zonal and meridional thermosphere neutral wind perturbations measured by
 280 FPI. (3) Subauroral TIDs in the vicinity of Millstone Hill. (4) SED measured by Mill-
 281 stone Hill and Poker Flat incoherent scatter radars. (5) Storm-time variation of midlat-
 282 itude ionospheric TEC and thermospheric O/N₂ over the North American sector.

283 4.1 Storm-time SAPS

284 As briefly mentioned above, SAPS refers to intense westward plasma flows (typ-
 285 ically greater than several hundred m/s) driven by a strong magnetically poleward elec-
 286 tric field in the subauroral ionosphere (Foster & Burke, 2002; Erickson et al., 2011). Fig-
 287 ure 2a shows the Northern Hemisphere polar view of TEC distribution at 21:30 UT on
 288 the storm day in the coordinates of magnetic local time (MLT) and geomagnetic lati-
 289 tude (MLAT), superposing DMSP F18 satellite cross-track ion velocity along its approx-
 290 imate dusk-dawn orbital path during 21:20–21:43 UT. There were two noticeable west-
 291 ward flow peaks around 60–68° MLAT in the dusk sector. SAPS was identified as the
 292 local peak westward flow at ~60° MLAT with a magnitude of ~1000 m/s, while the ion
 293 convection returning flow is seen as the other poleward peak separated by around 5°. More-
 294 over, SAPS was also collocated with moderately reduced background TEC (i.e., in/near
 295 the main ionospheric trough) when compared with its equatorward edge. The TEC re-
 296 duction may have resulted from an enhanced recombination rate associated with increased
 297 ion-neutral frictional heating due to large SAPS flows therein (Schunk, 1975), as well as
 298 SAPS-related large horizontal flux gradients.

299 Figure 2b shows line-of-sight Millstone Hill ISR plasma velocities for a full azimuth
 300 scan with 6° elevation together with the TEC map at 22:30 UT. SAPS flow signatures
 301 were clearly identified as the enhanced westward plasma flow of ~1000 m/s at around
 302 60–62° MLAT and 16–17 MLT, which is consistent with the result of DMSP cross-track
 303 velocity.

304 To better present ion convection and SAPS flow in the subauroral region to the north-
 305 west of Millstone Hill's location, we used line-of-sight plasma velocity west-looking data
 306 from the wide-coverage azimuth scan to the northwest of Millstone Hill between -70° and
 307 -10° azimuth angle and between 300–450 km in altitude, with the mean geodetic loca-
 308 tion at ~(51°N, 87°W). We then computed the magnetic eastward plasma drift compo-
 309 nent perpendicular to the magnetic field V_{perE} using a flow angle correction factor that
 310 assumes SAPS flow is aligned along constant magnetic latitude contours. This is a valid
 311 assumption near the base of SED as in this observational case and as introduced in sev-
 312 eral prior studies (Erickson et al., 2011; Zhang, Erickson, et al., 2017; Aa, Erickson, et
 313 al., 2020). In a similar manner, we also calculated the magnetic northward component
 314 of plasma drift perpendicular to the magnetic field V_{perN} . Specifically, V_{perN} was cal-
 315 culated from a poleward-looking subset of the line of sight velocity data where the ob-
 316 serving direction was approximately perpendicular to the field line near the magnetic merid-
 317 ian at the F region with the mean location at ~(52°N, 75°W). These settings and anal-
 318 ysis methods allow for sensitive determination of V_{perE} and V_{perN} vectors in the iono-

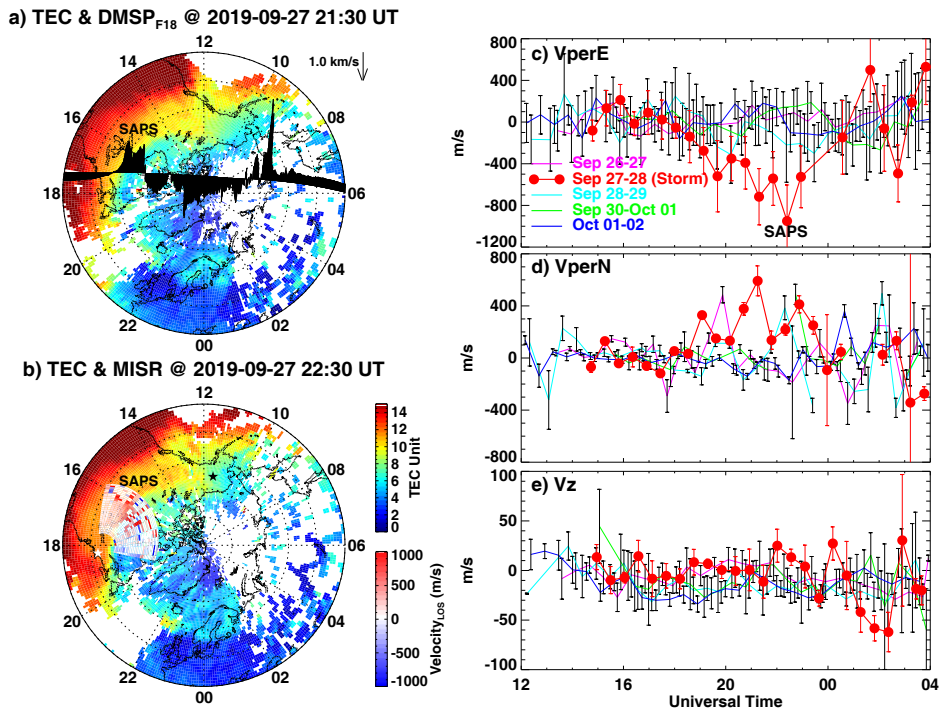


Figure 2. (a and b) Northern Hemisphere polar view of total electron content at 21:30 UT and 22:30 UT on 27 September 2019 in the coordinates of magnetic local time and geomagnetic latitude. Overlapping plots show (a) DMSP F18 cross-track ion velocities in the dawn-dusk plane during 21:20–21:43 UT and (b) line-of-sight plasma velocities for a full azimuth scan of Millstone Hill (white star) incoherent scatter radar during 22:15–22:31 UT. Concentric dashed circles are plotted in 10° interval with outermost one representing 40° MLAT. PFISR location is also marked by a black star. (c and d) V_{perE} (perpendicular eastward) and V_{perN} (perpendicular northward) plasma convection speed in the F-region estimated from the radar’s wide-coverage low-elevation experiment during five consecutive experiment days (see text). (e) Vertical ion drifts between 300–350 km at Millstone Hill derived from ISR zenith antenna measurements.

spheric F region with reliable accuracy and small uncertainty. For more details about the plasma velocity vector calculation, readers may refer to Zhang, Erickson, et al. (2017).

Using the above-mentioned methods and low-elevation Millstone Hill azimuth scans, Figures 2c and 2d show the temporal variation of the derived averaged eastward and northward plasma flow in the F region for each scan during five consecutive experiments days for this storm event. Results clearly show that the zonal ion velocity V_{perE} exhibited a significant westward drift reaching a maximum speed of ~ 1000 m/s at 22:30 UT on September 27. This drift was statistically significant and well beyond the uncertainty envelope calculated from other non-storm days during 20–24 UT. The enhanced plasma westward drift, together with the intense line-of-sight ion flow and DMSP cross-track drift in the North American subauroral area, clearly indicates the existence of strong SAPS and convection flow near the low-density main trough region to the northwest of Millstone Hill. These high-speed ion flows could influence local heating and cause thermospheric disturbances as will be discussed later.

333 Figure 2d shows that V_{perN} also exhibited daytime enhancements that were very
 334 evident between 19–23 UT (14–18 LT) on September 27, in configurations which are sig-
 335 natures of intermittent enhancements of penetration electric fields. In addition, Figures 2e
 336 displays the temporal variation of vertical ion drift between 300–350 km at Millstone Hill
 337 derived from zenith antenna measurements. We note that vertical drifts showed a large
 338 negative diversion at 01–03 UT on September 28, reaching a peak amplitude of around
 339 -60 m/s. This phenomenon occurred at 3–4 hours delay behind local SAPS, and could
 340 be related to zonal electric field response and/or meridional wind disturbances poten-
 341 tially associated with SAPS flows. We will further discuss this mechanism in the next
 342 subsection.

343 4.2 SAPS-related thermospheric wind response

344 Figure 3 presents Millstone Hill FPI nighttime measurements of zonal and merid-
 345 ional thermospheric neutral winds during September 25–30, 2019. Results, particularly
 346 in Figure 3c, indicate that during the storm main phase (September 27–28), the zonal
 347 wind began to exhibit a noticeable westward diversion from ~ 23 UT and remained strongly
 348 westward for the next 3–4 hours, reaching a maximum amplitude of ~ 230 m/s around
 349 01 UT. This feature did not occur on other non-storm days, and the storm time west-
 350 ward wind disturbance gradually diminished around 04–05 UT close to local midnight.

351 Figures 3f–3j display the temporal variation of the meridional wind. During the
 352 storm time shown in Figure 3h, the meridional wind component exhibited both strong
 353 equatorward and poleward surges in the local pre-midnight sector. Specifically, a consid-
 354 erable equatorward wind surge occurred after 00 UT on September 28. This equator-
 355 ward wind surge is an expected storm-time dynamic characteristic primarily driven by
 356 increased Joule heating and thermosphere expansion at high latitudes (Fuller-Rowell et
 357 al., 1994; Rishbeth, 1998). The equatorward wind surge reached a maximum magnitude
 358 of ~ 170 m/s at 0030–0100 UT on September 28 (~ 20 LT). This value is considerably
 359 larger than non-storm days since the storm-time wind surge was added to the background
 360 day-to-night neutral circulation pattern and was reinforced by the enhanced antisunward
 361 flow associated with expanded convection pattern (Buonsanto, 1999).

362 However, the equatorward neutral wind response to storm conditions also changed
 363 drastically poleward at 0130 UT and remained in this direction for about 2 hours be-
 364 fore returning equatorward. The maximum amplitude of this poleward wind surge was
 365 85 m/s at 0200–0230 UT, with a time delay of 1.5–2 hours following the peak westward
 366 wind and 3.5–4 hours following SAPS peak value. Despite minor storm forcing, these in-
 367 tense poleward wind surges and time-dependent responses are quite similar to that of
 368 the St. Patrick’s day storm in 2015 as shown by Zhang et al. (2015) and Guo et al. (2018),
 369 and will be further analyzed in the discussion section.

370 Beyond thermospheric effects, ionospheric effects of this poleward wind surge through
 371 ion-neutral coupling were manifested in vertical ion drifts shown in Figure 2e. As men-
 372 tioned in the previous subsection, during intervals between 01 and 03 UT on Septem-
 373 ber 28 with strong poleward wind, the vertical ion drift also exhibited a larger-than-average
 374 downward flow compared to reference days, while the zonal electric fields were quite small
 375 as inferred from both Figures 1d and 2d. This suggests that the neutral drag force as-
 376 sociated with the enhanced poleward wind may have played an important role in caus-
 377 ing enhanced downward ion drifts. Such effects are fully consistent with observations from
 378 the St. Patrick’s day storm results presented in (Zhang, Erickson, et al., 2017), and pro-
 379 vide a clear illustration that even a minor storm can trigger very similar I-T coupling
 380 features to that seen in severe storms.

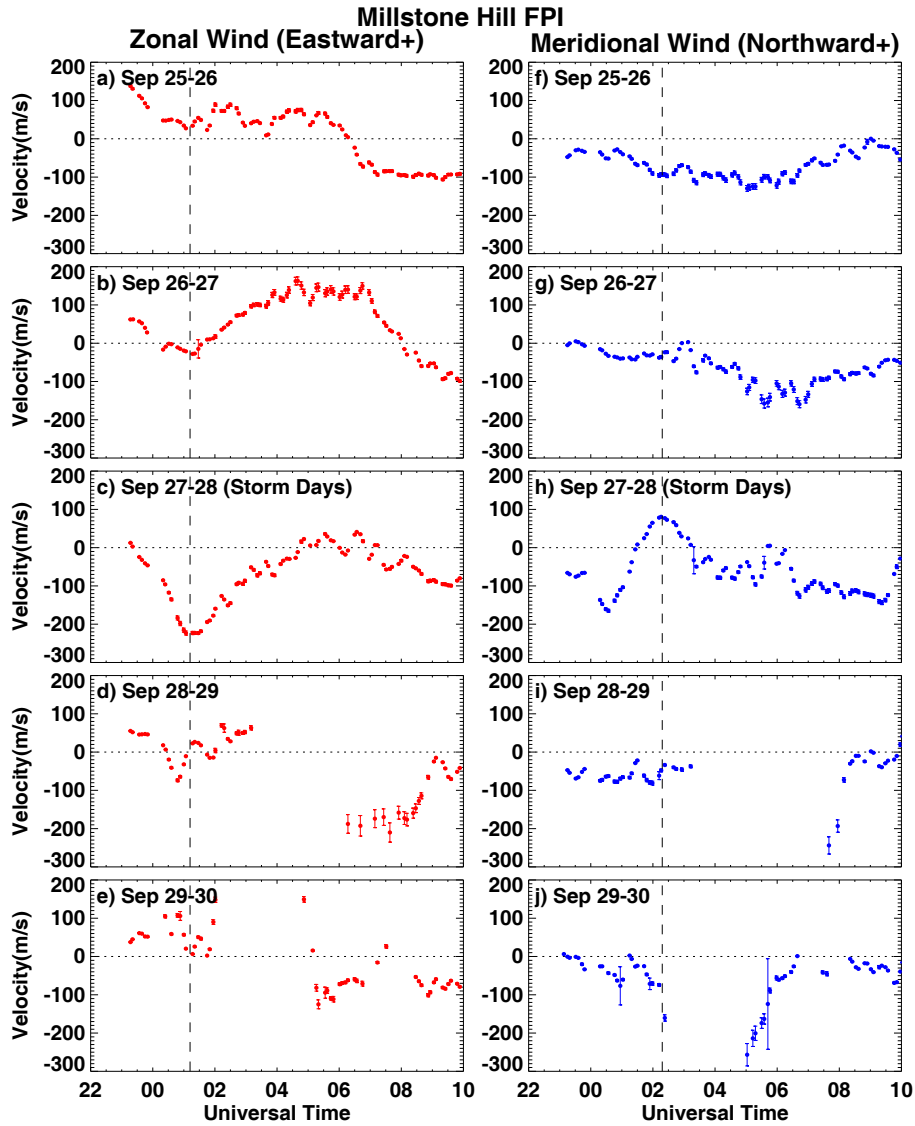


Figure 3. Millstone Hill FPI 630 nm (red-line) measurements of thermospheric neutral wind and corresponding uncertainties for zonal (a–e) and meridional (f–j) components during September 25–30, 2019. Vertical dashed lines mark the approximate time of intense westward and poleward wind surge during storm days shown in Figures 3c and 3h, respectively.

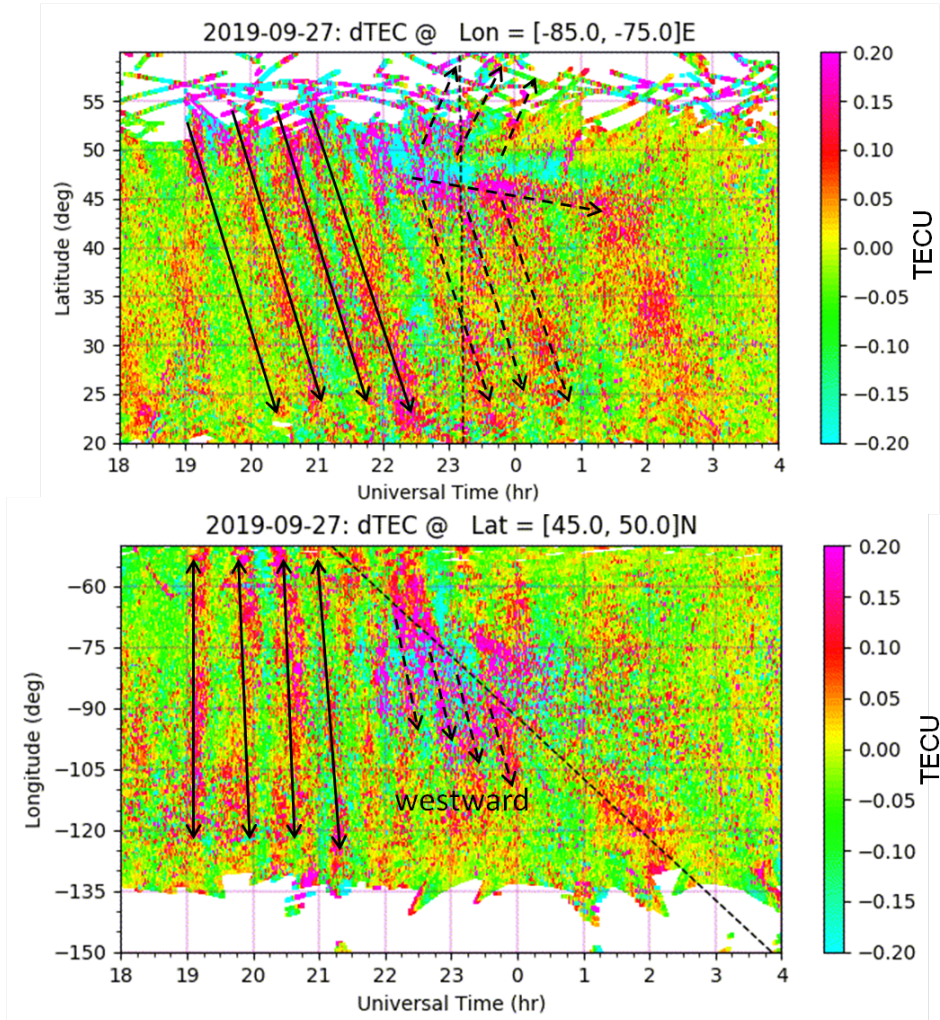


Figure 4. Temporal variation of the detrended TEC keogram as a function of (Top) latitude at 75–85°W and (bottom) longitude at 45–50°N in the North American sector on 27–28 September 2019. The dashed line represents the local sunset terminator. The solid lines with (top) arrows and (bottom) double-arrows mark equatorward propagating LSTIDs and their corresponding zonal wave fronts, respectively. The dashed lines with arrows mark the adjusted TID propagation pattern near dusk at times following the appearance of SAPS.

4.3 SAPS-related TIDs

Many prior storm-time TID studies have focused on the generation and propagation of large-scale TIDs (LSTIDs) primarily excited by high-latitude energy deposition due to enhanced Joule and particle heating (e.g., Ding et al., 2007; Zakharenkova et al., 2016; Jonah et al., 2018). In contrast, only a few studies in the literature have discussed the potential influence of SAPS on TID dynamics at subauroral latitudes (e.g., Guo et al., 2018; Zhang et al., 2019). Thus, in the current study, we will place emphasis on subauroral TIDs and further investigate their possible correlation with the existence of SAPS. Figure 4 shows two detrended TEC keograms as a function of latitude at 75–85°W and longitude at 45–50°N in the North American sector from 18 UT on September 27 to 04 UT on September 28. Significant wave-like TID structures can be clearly seen in those two panels. However, the TID structures exhibited quite different patterns in the pre-SAPS and post-SAPS intervals.

Firstly, equatorward propagating LSTIDs was the predominant pattern in the pre-SAPS interval between 19–22 UT. As the solar wind speed reached 600+ km/s at around 15:00 UT and Kp index reached 5+ at 18:00 UT, well-organized LSTIDs feature due to auroral-zone energy ingestion started to show since ~19:00 UT. In the top panel of Figure 4, at least four continuous large-scale wavefronts can be recognized. These LSTIDs propagated equatorward from auroral zone all the way to low-latitude region with an estimated period of ~40–50 min, horizontal velocity of ~800 m/s, and wavelength of 2000–2500 km. In the bottom panel, the corresponding LSTID wavefronts can be identified that aligned approximately along a zonal direction, spanning more than 60° in longitude from the U.S. west coast to east coast. These typical features and parameters values are consistent with prior storm-time LSTIDs studies (e.g., Zakharenkova et al., 2016; Jonah et al., 2018; Shiokawa et al., 2002).

However, the previous LSTIDs pattern went through a considerable adjustment between 22–00 UT around the dusk sector: the TID source region appeared to shift from the auroral zone to the subauroral region. Recall from Figure 2c that intense SAPS of ~1000 m/s occurred between 22–00 UT to the northwest of Millstone Hill. The top panel of Figure 4 also showed that divergent TID formats with both equatorward and some hint of poleward propagating components were generated in the subauroral region of 45–50°N following the appearance of the SAPS channel. This might suggest that the SAPS-related strong ion flow and frictional heating could effectively drive or adjust the TID pattern and caused the observed divergent propagating pattern. This phenomenon is similar to those indicated in Zhang et al. (2019) and will be further analyzed in the discussion section. Furthermore, the TID wavefronts also exhibited additional quasi-zonal propagating components of perturbation to the equatorward edge of the SAPS region. In particular, in the bottom panel of Figure 4, the previous double-arrow wavefronts started to rotate and break, exhibiting a clear westward propagating trend following the occurrence of SAPS as shown by the dashed arrows with an estimated velocity of ~600–800 m/s. This enhanced zonal perturbation with fast-moving features indicates that SAPS-related strong westward plasma flow might have generated the increased westward propagating components of LSTIDs.

4.4 SAPS-related SED

A clear SED feature in the North American sector was also observed by the Millstone Hill ISR in this minor but quite geo-effective storm. Specifically, Figure 5a shows *Ne* measurements for a full low-elevation azimuth scan of Millstone Hill ISR. A clear SED signature can be seen as a plume-like *Ne* elongation structure in the North American sector, marked with a red ellipse, starting from the location slightly north of the Great Lakes and extending westward/poleward in the afternoon sector. In addition, Figure 5b displays plasma line-of-sight velocity from Millstone Hill's field of view. A significant stream-

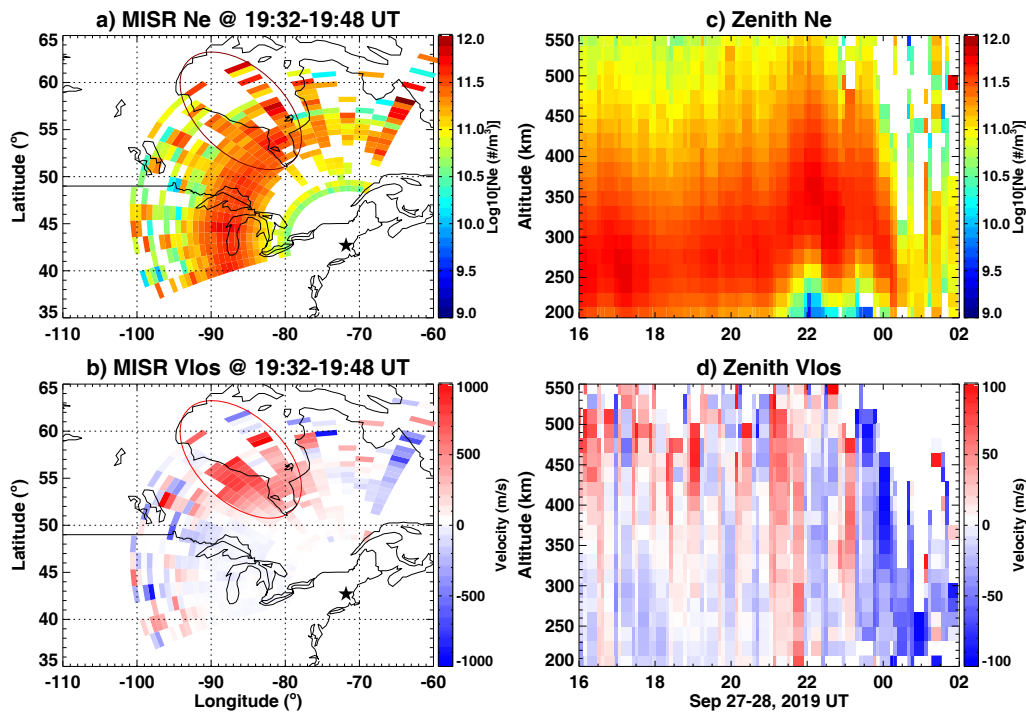


Figure 5. (a and b) Millstone Hill ISR (star) wide-coverage results of electron density and line-of-sight plasma velocities for a full azimuth scan during 19:32–19:48 UT on September 27. The red ellipse represents the signatures of SED. (c and d) Electron density and vertical plasma velocity as a function of altitude and universal time measured by zenith antenna of Millstone Hill incoherent scatter radar.

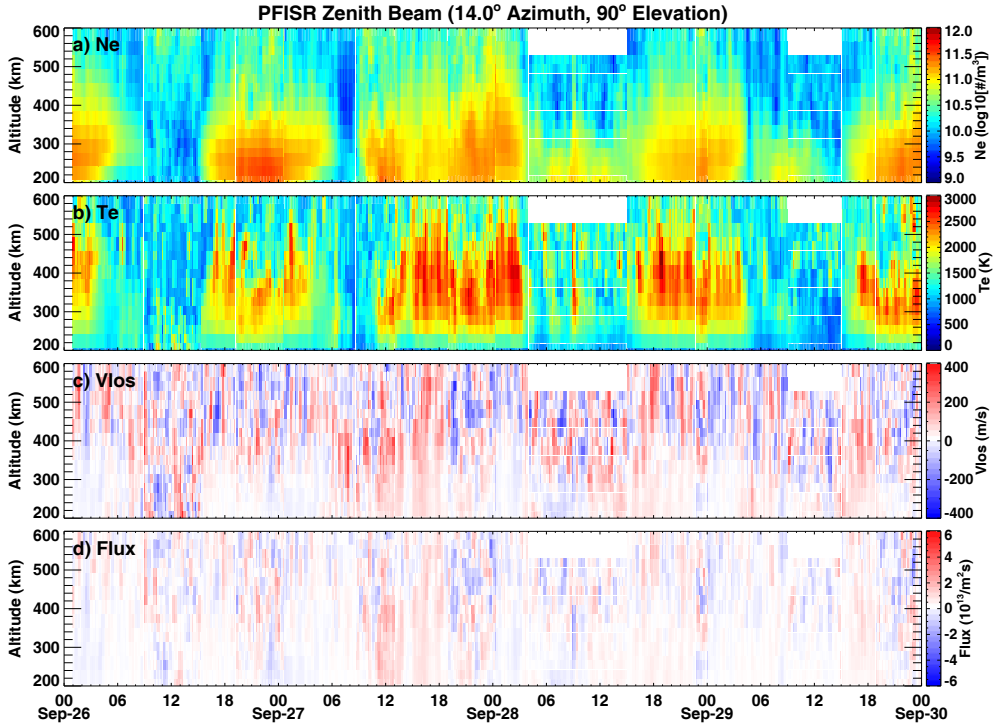


Figure 6. PFISR zenith beam observations in the long-pulse mode during 26–30 September 2019. (a–d) Altitudinal profiles of electron density (Ne), electron temperature (Te), line-of-sight velocity, and ion flux (i.e., the product of Ne and line-of-sight Velocity).

like sunward/poleward plasma flow of ~ 600 – 800 m/s in the F region can be seen approximately collocated with SED in the afternoon sector. This signature of enhanced Ne that associated with large sunward/poleward plasma flow is consistent with previous SED studies (Foster et al., 2007; Zou et al., 2013).

Moreover, SED and SAPS effects also appeared in zenith/vertical observations at Millstone Hill. In particular, Figures 5c and 5d show the temporal-altitudinal variation of Ne and vertical plasma velocity measured by zenith antenna. It can be seen that a strong upward ion drift of ~ 50 – 100 m/s appeared around 21–22 UT across the whole F region and topside ionosphere. This phenomenon of ion upflow in the midst of SAPS interval could be driven by enhanced frictional heating and associated expansion in the SAPS region, plus some contribution from penetration electric fields after IMF B_z turning southward. This ion upflow was followed by an electron density enhancement at 350 km and higher altitude due to the reduced recombination rate caused by the F-layer uplift in the topside ionosphere. The above-mentioned phenomenon is a marker of the local passage of SED over the Millstone Hill. Furthermore, the plasma velocity exhibited a large downward flow between 23–01 UT, possibly due to neutral drag effects from the poleward wind surge, as has been shown in Figures 2 and 3.

In this study, we also briefly examined PFISR observations to broaden and corroborate the storm-time ion-neutral coupling processes that were mentioned above, especially SED and SAPS-related effects. During this storm period, PFISR was operated in three different modes: an International Polar year mode, a MSWINDs mode, as well as

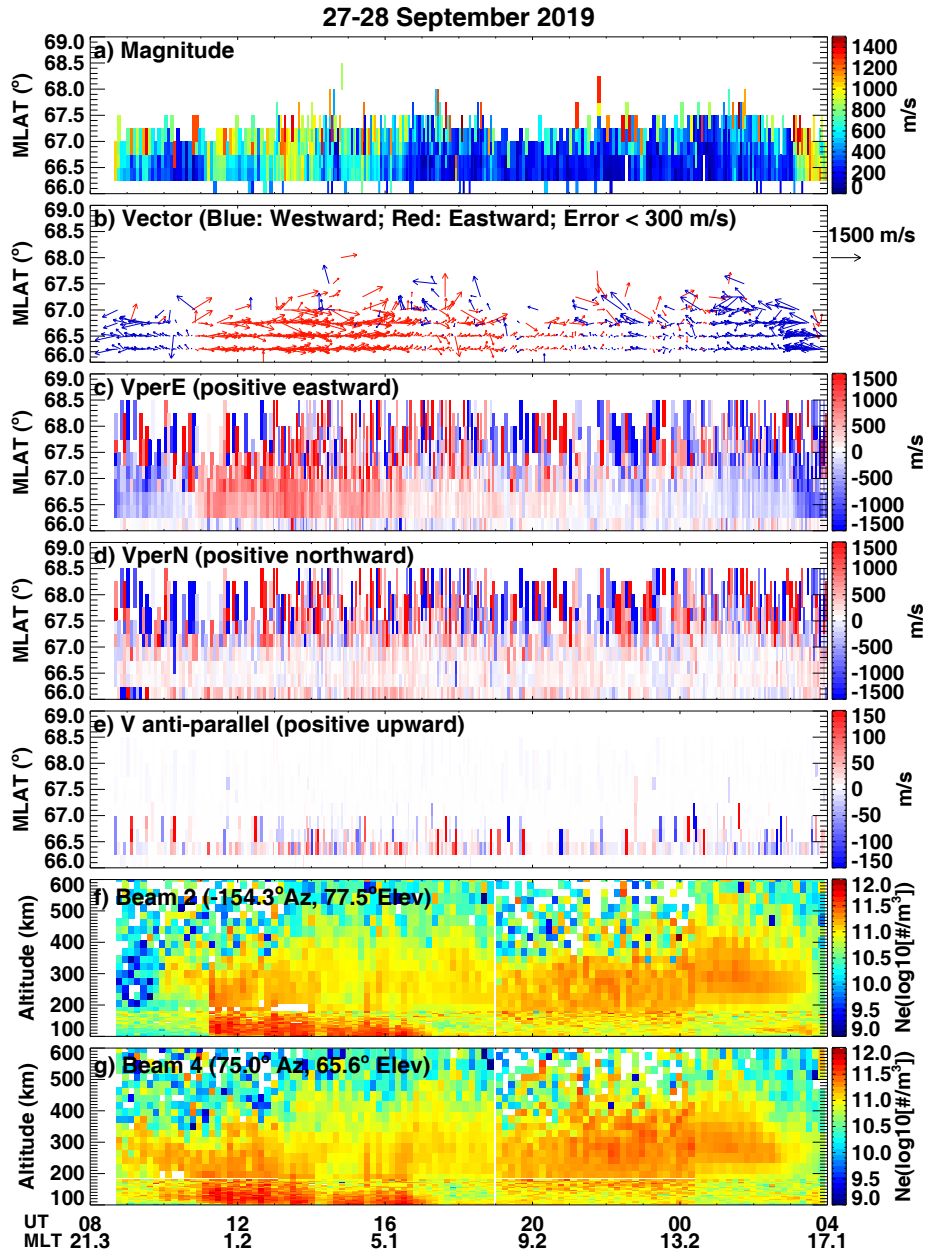


Figure 7. PFISR observations between 08 UT on September 27 and 04 UT on September 28. (a and b) The $E \times B$ convection flow magnitude and vector. (c–e) V_{perE} (perpendicular eastward), V_{perN} (perpendicular northward), and anti-parallel plasma flow speed along the filed line in the F-region. (f and g) Altitudinal profile of Ne for beam 2 and beam 4, respectively. Ne below 180 km is from the alternating code pulse measurement, while that above 180 km is from the long pulse measurement.

453 a world day 35 mode. There were four beams with common directions among those modes.
 454 Beam 1 was the zenith beam pointing to the magnetic north. Beam 2 was the southward
 455 beam that approximately pointed in the anti-parallel direction along the local magnetic
 456 field line. Beams 3 and 4 were pointing northwest and northeast, respectively. For more
 457 details on beam configurations, readers may refer to Zou et al. (2013). Figure 6 shows
 458 the altitudinal variation of zenith beam observations during 26–30 September 2019. Be-
 459 tween 23 UT on September 27 and 03 UT on September 28 among storm main phase,
 460 there was a modest electron density enhancement among 350–500 km comparing with
 461 the previous quiet day, and the corresponding hmF2 was slightly elevated around 50–
 462 100 km. These were local SED features near PFISR that related to the SAPS/SED sig-
 463 nature in TEC maps shown in Figure 2b. Moreover, the corresponding electron temper-
 464 ature within the interval of 23–03 UT also exhibited moderate enhancement of a few hun-
 465 dred K as compared to quiet time values. This enhanced electron temperature could par-
 466 tially come from the contribution of soft electron precipitation, which produces ioniza-
 467 tion in the F region and topside ionosphere as shown by previous modeling and obser-
 468 vational studies (e.g., Millward et al., 1999; Su et al., 1999; Zou et al., 2017).

469 To provide a more comprehensive analysis of the storm-time ionospheric convec-
 470 tion near Poker Flat, Figures 7a–7e shows the reconstructed vector velocity product from
 471 all PFISR beams between 08 UT on September 27 and 04 UT on September 28. These
 472 results include the $\mathbf{E} \times \mathbf{B}$ convection flow magnitude, vector distribution, V_{perE} , V_{perN} ,
 473 and anti-parallel plasma flow velocity as a function of UT and geomagnetic latitude. The
 474 convection flow at PFISR remained weak before 11 UT. With the passing of the stream
 475 interaction region and the beginning of the main phase, the convection pattern quickly
 476 expanded into the PFISR field-of-view, as showed by the large increase of convection flow
 477 speed between 12–17 UT in Figures 7a–7d. In comparison, PFISR zenith beam result
 478 (Figure 6c) also showed enhanced plasma vertical flow (>200 m/s) during 12–17 UT pre-
 479 dominantly due to the contribution from the $\mathbf{E} \times \mathbf{B}$ convection flow. In addition, during
 480 22–02 UT, the altitudinal profile observations from Beam 2 (Figure 7f) and Beam 4 (Fig-
 481 ure 7g) showed slightly elevated hmF2 and enhanced N_e . These phenomena were asso-
 482 ciated with northwestward plasma flow on the order of several hundreds m/s around 22:50
 483 UT as shown in Figures 7b–7d, which is consistent with the DMSP and Millstone Hill
 484 ISR measurements as shown in Figure 2. Zou et al. (2013) and Zou et al. (2014) indi-
 485 cated that these northwestward $\mathbf{E} \times \mathbf{B}$ flows collocated with SED can be either SAPS or
 486 enhanced convection flows. These played an important role for the density increase around
 487 PFISR due to their projected components in the vertical direction, which lifted plasma
 488 up to regions with lower recombination rate. Later, a much larger westward velocity en-
 489 hancement was registered at 02–04 UT, which is very similar to other past PFISR dusk-
 490 side SAPS observations (e.g., Lyons et al., 2015).

491 4.5 Positive and negative Ionosphere/thermosphere storm effects

492 We next investigate the storm-time variation of GNSS TEC and GOLD O/N₂ data
 493 to further analyze electrodynamic and thermospheric effects. To better understand storm-
 494 time variation, we removed the averaged TEC and O/N₂ reference values of seven quiet-
 495 time (all 3-hr Kp \leq 2+) days prior to the storm: September 19–23 and 25–26. We note
 496 that there was a minor Antarctic sudden stratosphere warming (SSW) event that occurred
 497 from late August to mid-September in 2019, which caused ionospheric TEC anomalies
 498 at low latitudes and in the southern hemisphere (Goncharenko et al., 2020). Given this
 499 factor, to minimize the effects on our study of SSW-related driving forces from the lower
 500 atmosphere, we will focus on discussing the mid-latitude ionosphere and thermosphere
 501 response only in the North American sector, and limit selection of reference days as in-
 502 dicated above.

503 Figures 8 shows ΔTEC and $\Delta\text{O/N}_2$ maps from GOLD observations in the American-
 504 Atlantic sector between 09–21 UT with a 3-hour interval on September 27 and 28, re-

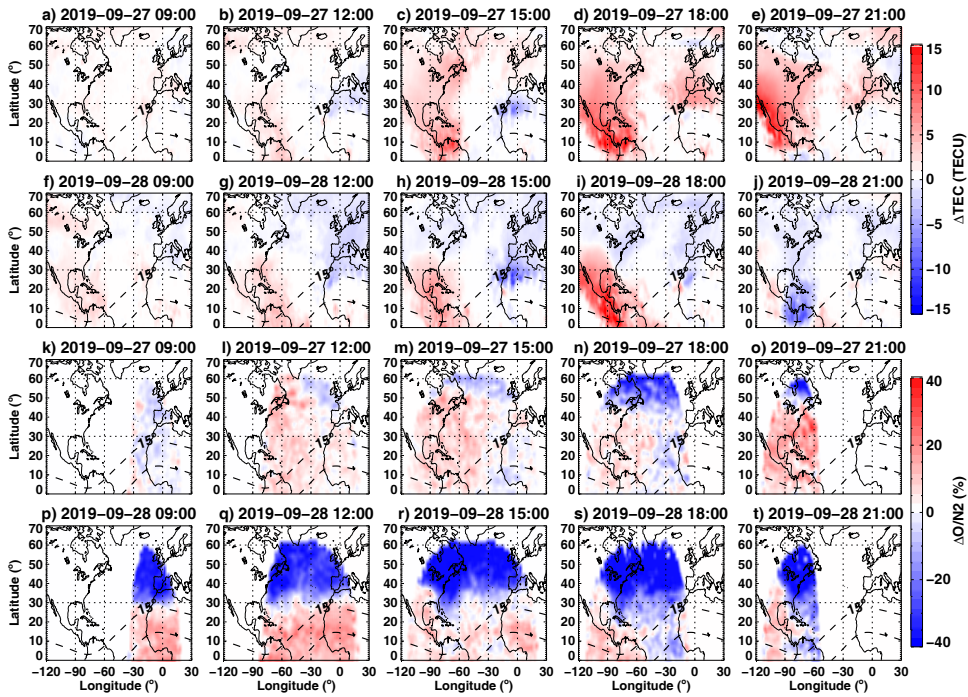


Figure 8. (a–j) ΔTEC and (k–t) $\Delta\text{O}/\text{N}_2$ variation in the Northern American-Atlantic sector between 09–21 UT with 3-hour interval on September 27 and 28, respectively. The geomagnetic equator and 15° line were marked by dashed lines.

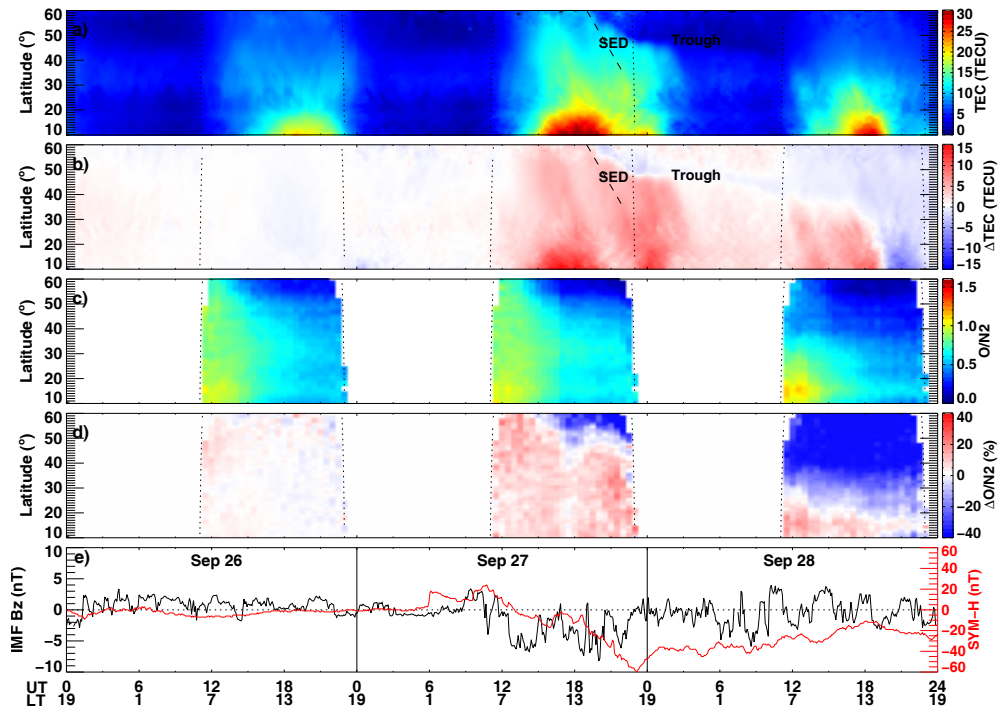


Figure 9. Keogram variations of (a) absolute TEC, (b) Δ TEC, (c) O/N_2 , and (d) $\Delta O/N_2$ as a function of geographic latitude and universal time in the North American sector that centered at $75^\circ W$ within $\pm 10^\circ$ in longitude during 26–28 September 2019. Dotted lines mark the local sunrise and sunset terminators. The SED feature is marked by slant dashed lines, and the storm-time deepened main trough structure is also labeled. (e) Temporal variation of IMF Bz (black) and SYM-H index (red), respectively.

505 spectively. Note that GOLD O/N₂ data is only available during the daytime. For the
506 midlatitude ionosphere over the North American region, TEC value showed a noticeable
507 enhancement of 5–10 TECU between 15–21 UT on September 27 within the main phase
508 of the storm, yet later showed a considerable reduction of 5–10 TECU between 12–21
509 UT on September 28 in the recovery phase. Similarly, the midlatitude O/N₂ ratio also
510 showed a modest increase of 10–20% on September 27 and a significant decrease of 20–
511 40% on September 28.

512 To better display storm-time ionosphere/thermosphere variation and to make a com-
513 parison with the above-mentioned Millstone Hill ISR/FPI campaign results, Figures 9a–
514 9d show the latitudinal-temporal variation of the absolute TEC, Δ TEC, O/N₂, and Δ O/N₂
515 values during 26–28 September centered on 75°W, close to the Millstone Hill longitude
516 in the North American sector. Note the mid-latitude ionospheric TEC and thermospheric
517 O/N₂ exhibited a long-duration positive storm effect for more than 12 hours during the
518 main phase on September 27, and TEC showed a persistent enhancement during local
519 nighttime on September 28 in the recovery phase. However, the subsequent variation of
520 mid-latitude TEC and O/N₂ showed a strong negative storm effect on the local daytime
521 of September 28. We will further analyze these opposite storm effects as well as asso-
522 ciated ionosphere-thermosphere processes.

523 Considerable positive deviation of ionospheric TEC from the reference values was
524 observed since \sim 13 UT on September 27 shortly after the beginning of the main phase.
525 In the meantime, the IMF Bz exhibited a modest southward excursion, followed by some
526 large fluctuations between negative and zero before reaching a minimum value of -8.2
527 nT at \sim 20 UT. Between 14–21 UT, the low-latitude TEC around the northern crest of
528 the equatorial ionization anomaly (EIA) showed a large daytime increase of 10–15 TECU.
529 Correspondingly, the mid-latitude ionospheric TEC between 20–50°N also exhibited a
530 considerable daytime increase of 5–10 TECU during the storm main phase, which con-
531 tinued for at least 12 hours before gradually subsided in the nighttime. Similarly, the
532 mid-latitude O/N₂ value showed a simultaneous 10–20% enhancement throughout the
533 daytime following the onset of the storm. Besides the electrodynamic effect of penetra-
534 tion electric field, this long-lived and synchronous mid-latitude positive I-T storm effect
535 could also be ascribed to two other possible mechanisms: (1) Downwelling of neutral atomic
536 oxygen caused by storm-time thermospheric circulation (Fuller-Rowell et al., 1994; Rish-
537 beth, 1998): The upwelling and divergence of the polar atmosphere heating caused O/N₂
538 decrease in high latitudes. In contrast, the altered thermospheric circulation leads to con-
539 vergence and downwelling of the neutral species through constant pressure level at low
540 and mid-latitudes, increasing atomic O density relative to molecular constituents and
541 thereby causing the TEC/*N*e enhancement (Buonsanto, 1999; Burns et al., 1995; Crow-
542 ley & Meier, 2008; Ngwira et al., 2012). (2) TEC enhancement caused by F-layer up-
543 lifting due to equatorward neutral wind surge (e.g., Burns et al., 1991; Mendillo, 2006;
544 Immel et al., 2001): An equatorward neutral wind surge at mid-latitudes is a common
545 storm-time feature of the thermosphere (Lu et al., 2008; Mendillo, 2006). Recall from
546 Figure 3 that strong equatorward neutral wind occurred near Millstone Hill around 23-
547 01 UT on September 27-28 before its poleward reversal. Moreover, the detrended TEC
548 results in Figure 4 showed noticeable large-scale TID structures starting at 18 UT. The
549 presence of equatorward neutral wind surge is consistent with the presence of these large-
550 scale TIDs. All this information collectively illustrates the equatorward propagation of
551 storm-induced high-latitude disturbances.

552 Furthermore, during the recovery phase on September 28, the daytime mid-latitude
553 ionosphere showed a considerable negative storm with the TEC being reduced 5–10 TECU
554 as shown in Figure 9b. Meanwhile, the storm-time modification of thermospheric com-
555 position also led to a 20–40% decrease of the O/N₂ ratio in the mid-latitude and a slight
556 increase of \sim 5–10% in the low latitudes. Theoretically, Fuller-Rowell et al. (1994) sug-
557 gested that the storm-time upwelling process should push N₂-rich air upward at mid/high

558 latitudes while pushing O-rich air downward at equatorial/low latitudes. Thus, the F-
559 region O/N₂ on a constant pressure surface would tend to exhibit a reduction at mid/high
560 latitudes and an enhancement at lower latitudes, especially during the storm recovery
561 phase (Prölss, 2008). This mechanism is quite relevant, especially considering GOLD ob-
562 servations are inherently equivalent to constant pressure surface observations (Eastes et
563 al., 2020). As shown in our results, this composition alteration at mid-latitudes tends
564 to increase the ion loss rate and cause the negative ionospheric storm therein (Prölss,
565 1976; Crowley et al., 2006). Moreover, this negative ionospheric storm expanded into the
566 low-latitude region in the local afternoon period after 20 UT (15 LT), leading to the sup-
567 pression of EIA crest densities of ~ 10 TECU amplitudes in the Northern Hemisphere.
568 In addition, besides the above-mentioned composition effect, the disturbed thermospheric
569 wind could also build up a disturbance dynamo electric field with a westward direction
570 in the daytime, which would suppress the quiet-time dynamo pattern and form a large
571 contribution to negative ionospheric storm effects in the low latitudes (Blanc & Rich-
572 mond, 1980; Kuai et al., 2016).

573 5 Discussion

574 5.1 SAPS-related thermospheric poleward wind surge

575 The Millstone Hill FPI and ISR measurements in this study demonstrate a strik-
576 ing phenomenon resulting from the effects of SAPS on ionosphere and thermosphere: a
577 strong poleward wind surge of ~ 85 m/s following an intense westward zonal wind of ~ 230 m/s
578 was observed in the post-SAPS period. This phenomenon could be explained by a causal
579 chain of subauroral ion-neutral coupling processes and relevant thermosphere dynam-
580 ics as follows: (1) Intense westward wind: Recall from Figure 2 that a significant SAPS
581 associated maximum westward ion drift of ~ 1000 m/s occurred around 22–24 UT on Septem-
582 ber 27 in the vicinity of Millstone Hill. In response, neutrals were subject to strong ion
583 drag effects in the SAPS channel via ion-neutral friction and would subsequently form
584 large westward winds, as have been observed and modeled in several prior studies (e.g.,
585 Ferdousi et al., 2019; H. Wang et al., 2011, 2018; W. Wang et al., 2012; Zhang et al., 2015).
586 Due to the time scales of these effects, there was a 2–3 hours time delay between the west-
587 ward neutral wind disturbance and SAPS flow both for their initiation and peak responses.
588 (2) Strong poleward wind surge: Besides our result, a similar SAPS event with poleward
589 wind surge was observed by Zhang et al. (2015) and simulated by Guo et al. (2018) for
590 the 2015 St. Patrick’s day storm. Both studies indicated that the Coriolis force on the
591 westward zonal wind contributed to its northward rotating and subsequent poleward surge.
592 Moreover, Guo et al. (2018) suggested that the pressure gradient due to storm-time TAD/TID
593 related to auroral and frictional heating could play a dominant role in triggering such
594 a poleward wind surge. Shiokawa et al. (2003) also observed poleward wind enhancement
595 at mid-latitudes during a major storm event and indicated that it correlated with LSTIDs.
596 Recall from Figure 4 that both significant auroral-induced TIDs as well as subauroral
597 TID feature with divergent propagation components were observed during the storm main
598 phase before the appearance of poleward wind. The simulation in Zhang et al. (2015)
599 indicated the Coriolis forcing was able to establish the poleward wind in 1–2 hours, con-
600 sistent with both the observed time lag from a zonal wind enhancement to poleward wind
601 evolution and with the observed poleward wind peak velocity. However, this fundamen-
602 tal forcing resulted in only a smooth and gradual increase in the poleward wind. In the
603 end, therefore, TADs/TIDs originated either by auroral or subauroral processes can pro-
604 vide a swift poleward wind surge but would need to meet specific excitation and prop-
605 agation conditions to match the observed timing of the wind surge.

5.2 SAPS induced TIDs

Coincident occurrence of westward propagating TIDs and strong SAPS was found in the North American subauroral region near Millstone Hill ISR. This phenomenon is similar to that reported in Zhang et al. (2019), and the generation mechanisms of these TIDs and their connection with SAPS might be explained as follows: (1) Gravity waves due to SAPS-induced frictional heating: It is known that SAPS will cause significant frictional heating due to large ion-neutral relative velocity therein (Anderson et al., 1991; Rodger, 2008). Guo et al. (2018) indicated that the intense frictional heating effect due to SAPS could cause neutral temperature and composition changes, resulting in acoustic-gravity waves that propagate away in the form of TAD/TIDs near the SAPS region. (2) Amplification of the Perkins instability growth rate due to SAPS electric field: Besides gravity waves, electrodynamic forces under a favorable condition of the Perkins instability (Perkins, 1973) could also explain the formation of mid-latitude medium-scale TIDs, though Perkins instability growth rates are usually quite small (Kelley & Fukao, 1991). Zhang et al. (2019) indicated that a strong magnetically poleward SAPS electric field could effectively amplify the Perkins instability growth rate, so that TIDs with a strong polarization electric field variation can be generated in the subauroral region. A future theoretical study is needed to further address the mechanism.

5.3 Interplay between SAPS and SED

A notable SED feature associated with dusktime positive ionospheric storm conditions can be seen in Figures 9a and 9b as a plume-like large-amplitude TEC structure marked by dashed lines. This SED feature was also observed by the Millstone Hill incoherent scatter radar as shown in Figure 5. SED occurrence during such a minor but geo-effective storm is quite interesting, and it can potentially be ascribed to a combination of the following mechanisms: (1) Zonal ion transport driven by SAPS or enhanced convection flow: The poleward edge of SED is collocated with the equatorward wall of the deepened main trough where intense SAPS flow existed as shown in Figure 2. Moreover, Figure 9b shows that the storm-time main trough feature was much more pronounced than the previous quiet day. This indicates the presence of SAPS, since the enhanced ion temperature within SAPS could accelerate the recombination rate therein (Rodger, 2008; Aa, Zou, et al., 2020). Under these factors, plume materials could be effectively carried sunward from the nightside to the dayside in the SAPS overlapping region (Foster et al., 2007). Figures 9a and 9b also showed that the main trough channel was significantly deepened and pushed equatorward around dusktime, indicating the equatorward expansion of the convection pattern. Foster (1993) suggested that the expansion of high-latitude convection in the afternoon sector can pick up high-density plasma on its equatorward edge and transport it toward the cusp. (2) Ion transport across wide latitudinal regions: Some prior studies indicated that the peak of equatorial ionization anomaly could be pushed toward higher latitudes due to enhanced fountain effect though this effect is most likely a severe storm feature (e.g., Gardner et al., 2018; Kelley et al., 2004; Tsurutani et al., 2004). In our results, Figure 8b show synchronous mid-latitude and low-latitude TEC enhancement of ~ 10 TECU around the dusk sector. It is likely therefore that the TEC enhancement within the SED extended from the EIA crest region to higher latitudes, providing a seed population for density increases to be carried by SAPS and/or convection flow.

6 Conclusions

In this study, we have investigated SAPS-related ion-neutral coupling processes and related mid-latitude ionosphere and thermosphere responses during a modest but geo-effective storm on 27–28 September 2019 around the recent deep solar minimum. The effects of SAPS on midlatitude electrodynamics and dynamics in the North American

656 sector were comprehensively analyzed using Millstone Hill incoherent scatter radar data,
657 FPI measurements, GNSS TEC, DMSP cross-track drifts, and PFISR measurements,
658 as well as GOLD O/N₂ data. A number of salient and interesting features of ionospheric/thermospheric
659 disturbances during the storm were recognized and summarized as follows:

660 1. Both ground-based incoherent scatter radar and DMSP cross-track measurements
661 showed evidence of strong SAPS flow of 1000 m/s in the North American sector during
662 20–24 UT on September 27. Deepened main trough structure associated with SAPS
663 was observed in GNSS TEC data, likely due to enhanced frictional heating and ion loss caused
664 by SAPS. Considerable ion upflow of ~50 m/s in the F region was also measured at Mill-
665 stone Hill during a SAPS-influenced interval in the local afternoon.

666 2. Around two hours after SAPS peak flow, a westward neutral wind peak of 230 m/s
667 was observed by the FPI at Millstone Hill during 00–01 UT on September 28, driven by
668 SAPS-related accumulative ion-drag effects. Later, the meridional wind showed a dras-
669 tic turning from -170 m/s (equatorward) at 0030 UT to 85 m/s (poleward) at 0230 UT.
670 This unusual poleward wind surge was possibly caused by the combining effects of the
671 Coriolis force on the enhanced westward neutral wind and pressure gradients due to storm-
672 time TAD/TIDs. The neutral drag effect of this poleward wind surge also caused con-
673 current large downward ion flow of 50–100 m/s at Millstone Hill.

674 3. During the storm main phase, intense daytime LSTIDs were generated in the
675 auroral zone and propagated equatorward in the North American sector with a wave-
676 length of 2000–2500 km and periods of 40–50 min. However, the occurrence of dusktime
677 SAPS caused significant changes to TID propagation and excitation. Under the influ-
678 ence of SAPS frictional heating and electric field, the previous zonal wavefronts started
679 to rotate and break, exhibiting prominent divergent patterns with additional westward
680 propagating TID components.

681 4. A significant SED feature was collectively observed by (a) GNSS TEC as an en-
682 hanced TEC structure and (b) Millstone Hill ISR as an enhanced Ne band with upward
683 ion drift of 50 m/s in the local afternoon sector. In addition, the main trough and SAPS
684 were simultaneously observed near the poleward edge of SED, and SED was also observed
685 by PFISR associated with northwestward plasma flows. These facts suggest that a com-
686 bination of zonal ion transport driven by strong westward plasma flow and $\mathbf{E} \times \mathbf{B}$ plasma
687 drift projected in the vertical direction, with some contribution from ion transportation
688 across latitudes, collectively generated this considerable storm-time SED feature.

689 5. A prolonged positive ionospheric and thermospheric storm feature occurred at
690 mid-latitudes for more than 12 hours during the main phase and early part of the recov-
691 ery phase, with TEC enhancement of ~5–10 TECU and column O/N₂ ratio increase of
692 ~10–20%. This positive I-T storm effect could be collectively generated by atomic oxy-
693 gen downwelling caused by storm-time thermospheric circulation, combined with plasma
694 uplifting due to the equatorward neutral wind and enhanced storm-time TAD/TIDs.

695 6. A synchronous negative storm effect across the mid-latitude ionosphere and ther-
696 mosphere was observed during the later half of the recovery phase, with TEC reduction
697 of ~5–10 TECU and column O/N₂ ratio decrease of ~20–40%. This phenomenon could
698 be largely caused by thermospheric composition change, plus some contribution from dis-
699 turbance dynamo electric field.

700 In aggregate, the presence of these substantial, and perhaps unexpected, ionosphere
701 and thermosphere effects during a deep solar minimum, modest strength geomagnetic
702 storm provide compelling evidence of the significant role of magnetosphere-ionosphere-
703 thermosphere coupling in upper atmosphere dynamics. Future modeling and observa-
704 tional studies are encouraged to further explore the range of ionospheric and thermospheric
705 variability such coupling can provide under an expanded range of solar and geomagnetic
706 conditions.

Data Availability Statement

Millstone Hill incoherent scatter radar observation and GNSS TEC data products are provided to the community through the Madrigal distributed data system at (<http://cedar.openmadrigal.org/>) by the Massachusetts Institute of Technology (MIT) under NSF grant AGS-1952737. The PFISR data are available at the SRI AMISR database (<https://data.amisr.com/database/61/>) and the Madrigal CEDAR database (<http://cedar.openmadrigal.org/>). The FPI data are available at the Madrigal CEDAR database (<http://cedar.openmadrigal.org/>). The DMSP SSIES data are available at NOAA NGDC (satdat.ngdc.noaa.gov/dmsp/) and the Madrigal CEDAR database (<http://cedar.openmadrigal.org/>). The GOLD data are provided to the public by NASA/GOLD mission science team (<https://gold.cs.ucf.edu/>). The solar and geophysical parameters data is acquired from NASA/GSFC's Space Physics Data Facility's OMNIWeb service (<https://cdaweb.gsfc.nasa.gov/>) and Kyoto world data center for Geomagnetism (<http://wdc.kugi.kyoto-u.ac.jp/>).

Acknowledgments

Millstone Hill incoherent scatter radar observation and GNSS TEC data are part of the U.S. NSF Geospace Facility program under a cooperative agreement AGS-1952737 with Massachusetts Institute of Technology, which also supported in part research activity by MIT Haystack Observatory members. SRZ and AJC acknowledge the AFOSR support for the MURI Project FA9559-16-1-0364; and AJC, SRZ and LPG acknowledge the ONR Grant N00014-17-1-2186. Data for the TEC processing is provided from the following organizations: The Crustal Dynamics Data Information System (CDDIS), the Scripps Orbit and Permanent Array Center (SOPAC), the Continuously Operating Reference System (CORS), the EUREF Permanent GNSS network (EPN), the University NAVSTAR Consortium (UNAVCO), Institut Geographique National in France (IGN), the Brazilian Network for Continuous Monitoring (RBMC), National Geodetic Survey, Instituto Brasileiro de Geografia e Estatística, RAMSAC CORS of Instituto Geográfico Nacional de la República Argentina, Arecibo Observatory, Low-Latitude Ionospheric Sensor Network (LISN), Topcon Positioning Systems, Inc., Canadian High Arctic Ionospheric Network, Centro di Ricerche Sismologiche, Système d'Observation du Niveau des Eaux Littorales (SONEL), RENAG : REseau National GPS permanent, GeoNet - the official source of geological hazard information for New Zealand, GNSS Reference Networks, Finnish Meteorological Institute, SWEPOS - Sweden.

References

- Aa, E., Erickson, P. J., Zhang, S.-R., Zou, S., Coster, A. J., Goncharenko, L. P., & Foster, J. C. (2020, October). A Statistical Study of the Subauroral Polarization Stream Over North American Sector Using the Millstone Hill Incoherent Scatter Radar 1979-2019 Measurements. *Journal of Geophysical Research: Space Physics*, *125*(10), e28584. doi: 10.1029/2020JA028584
- Aa, E., Zou, S., Erickson, P. J., Zhang, S.-R., & Liu, S. (2020, March). Statistical Analysis of the Main Ionospheric Trough Using Swarm in Situ Measurements. *Journal of Geophysical Research: Space Physics*, *125*(3), e27583. doi: 10.1029/2019JA027583
- Aa, E., Zou, S., Ridley, A., Zhang, S., Coster, A. J., Erickson, P. J., ... Ren, J. (2019, February). Merging of Storm Time Midlatitude Traveling Ionospheric Disturbances and Equatorial Plasma Bubbles. *Space Weather*, *17*(2), 285-298. doi: 10.1029/2018SW002101
- Anderson, P. C., Heelis, R. A., & Hanson, W. B. (1991, Apr). The ionospheric signatures of rapid subauroral ion drifts. *Journal of Geophysical Research*, *96*(A4), 5785-5792. doi: 10.1029/90JA02651
- Astafyeva, E., Bagiya, M. S., Förster, M., & Nishitani, N. (2020, March). Unprece-

- 758 dented Hemispheric Asymmetries During a Surprise Ionospheric Storm: A
 759 Game of Drivers. *Journal of Geophysical Research: Space Physics*, 125(3),
 760 e27261. doi: 10.1029/2019JA027261
- 761 Astafyeva, E., Zakharenkova, I., & Förster, M. (2015, October). Ionospheric re-
 762 sponse to the 2015 St. Patrick's Day storm: A global multi-instrumental
 763 overview. *Journal of Geophysical Research: Space Physics*, 120(10), 9023-
 764 9037. doi: 10.1002/2015JA021629
- 765 Astafyeva, E., Zakharenkova, I., Huba, J. D., Doornbos, E., & van den IJssel, J.
 766 (2017, November). Global Ionospheric and Thermospheric Effects of the June
 767 2015 Geomagnetic Disturbances: Multi-Instrumental Observations and Model-
 768 ing. *Journal of Geophysical Research: Space Physics*, 122(11), 11,716-11,742.
 769 doi: 10.1002/2017JA024174
- 770 Balan, N., Shiokawa, K., Otsuka, Y., Kikuchi, T., Vijaya Lekshmi, D., Kawamura,
 771 S., ... Bailey, G. J. (2010, February). A physical mechanism of positive
 772 ionospheric storms at low latitudes and midlatitudes. *Journal of Geophysical
 773 Research: Space Physics*, 115(A2), A02304. doi: 10.1029/2009JA014515
- 774 Blanc, M., & Richmond, A. D. (1980, April). The ionospheric disturbance
 775 dynamo. *Journal of Geophysical Research*, 85(A4), 1669-1686. doi:
 776 10.1029/JA085iA04p01669
- 777 Buonsanto, M. J. (1999, April). Ionospheric Storms — A Review. *Space Sci. Review*,
 778 88, 563-601. doi: 10.1023/A:1005107532631
- 779 Buonsanto, M. J., Foster, J. C., & Sipler, D. P. (1992, Feb). Observations
 780 From Millstone Hill During the Geomagnetic Disturbances of March and
 781 April 1990. *Journal of Geophysical Research*, 97(A2), 1225-1243. doi:
 782 10.1029/91JA02428
- 783 Burns, A. G., Killeen, T. L., Deng, W., Carignan, G. R., & Roble, R. G. (1995, Au-
 784 gust). Geomagnetic storm effects in the low- to middle-latitude upper thermo-
 785 sphere. *Journal of Geophysical Research*, 100(A8), 14673-14692. doi: 10.1029/
 786 94JA03232
- 787 Burns, A. G., Killeen, T. L., & Roble, R. G. (1991, August). a theoretical study
 788 of thermospheric composition perturbations during a impulsive geomag-
 789 netic storm. *Journal of Geophysical Research*, 96(A8), 14153-14167. doi:
 790 10.1029/91JA00678
- 791 Coster, A. J., & Foster, J. (2007). Space-weather impacts of the sub-auroral polar-
 792 ization stream. *URSI Radio Science Bulletin*, 2007(321), 28-36.
- 793 Crowley, G., Hackert, C. L., Meier, R. R., Strickland, D. J., Paxton, L. J., Pi, X., ...
 794 Wene, G. (2006, October). Global thermosphere-ionosphere response to onset
 795 of 20 November 2003 magnetic storm. *Journal of Geophysical Research: Space
 796 Physics*, 111(A10), A10S18. doi: 10.1029/2005JA011518
- 797 Crowley, G., & Meier, R. R. (2008, January). Disturbed O/N₂ ratios and their
 798 transport to middle and low latitudes. *Washington DC American Geophysical
 799 Union Geophysical Monograph Series*, 181, 221-234. doi: 10.1029/181GM20
- 800 Deng, W., Killeen, T. L., Burns, A. G., Roble, R. G., Slavin, J. A., & Wharton,
 801 L. E. (1993, May). The effects of neutral inertia on ionospheric currents in
 802 the high-latitude thermosphere following a geomagnetic storm. *Journal of
 803 Geophysical Research*, 98(A5), 7775-7790. doi: 10.1029/92JA02268
- 804 Ding, F., Wan, W., Ning, B., & Wang, M. (2007, June). Large-scale traveling
 805 ionospheric disturbances observed by GPS total electron content during the
 806 magnetic storm of 29-30 October 2003. *Journal of Geophysical Research: Space
 807 Physics*, 112(A6), A06309. doi: 10.1029/2006JA012013
- 808 Doherty, P., Coster, A. J., & Murtagh, W. (2004, December). Space weather effects
 809 of OctoberNovember 2003. *GPS Solutions*, 8, 267-271. doi: 10.1007/s10291
 810 -004-0109-3
- 811 Eastes, R. W., McClintock, W. E., Burns, A. G., Anderson, D. N., Andersson, L.,
 812 Aryal, S., ... Woods, T. N. (2020, July). Initial Observations by the GOLD

- 813 Mission. *Journal of Geophysical Research: Space Physics*, 125(7), e27823. doi:
814 10.1029/2020JA027823
- 815 Eastes, R. W., Solomon, S. C., Daniell, R. E., Anderson, D. N., Burns, A. G., Eng-
816 land, S. L., ... McClintock, W. E. (2019, August). Global-Scale Observations
817 of the Equatorial Ionization Anomaly. *Geophysical Research Letters*, 46(16),
818 9318-9326. doi: 10.1029/2019GL084199
- 819 Erickson, P., Goncharenko, L., Nicolls, M., Ruohoniemi, M., & Kelley, M. (2010).
820 Dynamics of north american sector ionospheric and thermospheric re-
821 sponse during the november 2004 superstorm. *Journal of Atmospheric and*
822 *Solar-Terrestrial Physics*, 72(4), 292-301. doi: https://doi.org/10.1016/
823 j.jastp.2009.04.001
- 824 Erickson, P. J., Beroz, F., & Miskin, M. Z. (2011, Mar). Statistical characterization
825 of the American sector subauroral polarization stream using incoherent scatter
826 radar. *Journal of Geophysical Research: Space Physics*, 116, A00J21. doi:
827 10.1029/2010JA015738
- 828 Evans, J. V. (1969). Theory and practice of ionosphere study by thomson scatter
829 radar. *Proceedings of the IEEE*, 57(4), 496-530. doi: 10.1109/PROC.1969
830 .7005
- 831 Ferdousi, B., Nishimura, Y., Maruyama, N., & Lyons, L. R. (2019, March). Subau-
832 roral Neutral Wind Driving and Its Feedback to SAPS During the 17 March
833 2013 Geomagnetic Storm. *Journal of Geophysical Research: Space Physics*,
834 124(3), 2323-2337. doi: 10.1029/2018JA026193
- 835 Foster, J. C. (1993, February). Storm time plasma transport at middle and high
836 latitudes. *Journal of Geophysical Research: Space Physics*, 98(A2), 1675-1690.
837 doi: 10.1029/92JA02032
- 838 Foster, J. C., & Burke, W. J. (2002). SAPS: A new categorization for sub-auroral
839 electric fields. *EOS Transactions*, 83(36), 393. doi: 10.1029/2002EO000289
- 840 Foster, J. C., Coster, A. J., Erickson, P. J., Holt, J. M., Lind, F. D., Rideout, W.,
841 ... Rich, F. J. (2005, Sep). Multiradar observations of the polar tongue of
842 ionization. *Journal of Geophysical Research: Space Physics*, 110(A9), A09S31.
843 doi: 10.1029/2004JA010928
- 844 Foster, J. C., Rideout, W., Sandel, B., Forrester, W. T., & Rich, F. J. (2007,
845 March). On the relationship of SAPS to storm-enhanced density. *Jour-
846 nal of Atmospheric and Solar-Terrestrial Physics*, 69(3), 303-313. doi:
847 10.1016/j.jastp.2006.07.021
- 848 Foster, J. C., & Vo, H. B. (2002, Dec). Average characteristics and activity depen-
849 dence of the subauroral polarization stream. *Journal of Geophysical Research:
850 Space Physics*, 107(A12), 1475. doi: 10.1029/2002JA009409
- 851 Fuller-Rowell, T. J., Codrescu, M. V., Moffett, R. J., & Quegan, S. (1994, March).
852 Response of the thermosphere and ionosphere to geomagnetic storms. *Journal
853 of Geophysical Research*, 99(A3), 3893-3914. doi: 10.1029/93JA02015
- 854 Galperin, Y., Ponomarov, Y., & Zosinova, A. (1974). Plasma convection in polar
855 ionosphere. *Annales de Geophysique*, 30(1-7).
- 856 Gardner, L. C., Schunk, R. W., Scherliess, L., Eccles, V., Basu, S., & Valladeres,
857 C. (2018, October). Modeling the Midlatitude Ionosphere Storm-Enhanced
858 Density Distribution With a Data Assimilation Model. *Space Weather*, 16(10),
859 1539-1548. doi: 10.1029/2018SW001882
- 860 Goncharenko, L. P., Harvey, V. L., Greer, K. R., Zhang, S. R., & Coster, A. J.
861 (2020, August). Longitudinally Dependent Low-Latitude Ionospheric Distur-
862 bances Linked to the Antarctic Sudden Stratospheric Warming of September
863 2019. *Journal of Geophysical Research: Space Physics*, 125(8), e28199. doi:
864 10.1029/2020JA028199
- 865 Guo, J.-P., Deng, Y., Zhang, D.-H., Lu, Y., Sheng, C., & Zhang, S.-R. (2018,
866 March). The Effect of Subauroral Polarization Streams on Ionosphere and
867 Thermosphere During the 2015 St. Patrick's Day Storm: Global Ionosphere-

- 868 Thermosphere Model Simulations. *Journal of Geophysical Research (Space*
 869 *Physics)*, 123(3), 2241-2256. doi: 10.1002/2017JA024781
- 870 Hairston, M., Coley, W. R., & Stoneback, R. (2016, November). Responses in the
 871 polar and equatorial ionosphere to the March 2015 St. Patrick Day storm.
 872 *Journal of Geophysical Research: Space Physics*, 121(11), 11,213-11,234. doi:
 873 10.1002/2016JA023165
- 874 Huang, C.-S., Rich, F. J., & Burke, W. J. (2010, August). Storm time elec-
 875 tric fields in the equatorial ionosphere observed near the dusk meridian.
 876 *Journal of Geophysical Research: Space Physics*, 115(A8), A08313. doi:
 877 10.1029/2009JA015150
- 878 Huang, C.-S., Wilson, G. R., Hairston, M. R., Zhang, Y., Wang, W., & Liu, J.
 879 (2016). Equatorial ionospheric plasma drifts and o+ concentration enhance-
 880 ments associated with disturbance dynamo during the 2015 st. patrick's day
 881 magnetic storm. *Journal of Geophysical Research: Space Physics*, 121(8),
 882 7961-7973. doi: 10.1002/2016JA023072
- 883 Huba, J. D., Sazykin, S., & Coster, A. (2017, January). SAMI3-RCM simulation of
 884 the 17 March 2015 geomagnetic storm. *Journal of Geophysical Research: Space*
 885 *Physics*, 122(1), 1246-1257. doi: 10.1002/2016JA023341
- 886 Hunsucker, R. D. (1982, May). Atmospheric Gravity Waves Generated in the High-
 887 Latitude Ionosphere: A Review. *Reviews of Geophysics and Space Physics*, 20,
 888 293. doi: 10.1029/RG020i002p00293
- 889 Immel, T. J., Crowley, G., Craven, J. D., & Roble, R. G. (2001, August). Dayside
 890 enhancements of thermospheric O/N₂ following magnetic storm onset. *Journal*
 891 *of Geophysical Research: Space Physics*, 106(A8), 15471-15488. doi: 10.1029/
 892 2000JA000096
- 893 Jimoh, O., Lei, J., Zhong, J., Owolabi, C., Luan, X., & Dou, X. (2019, November).
 894 Topside Ionospheric Conditions During the 7-8 September 2017 Geomagnetic
 895 Storm. *Journal of Geophysical Research: Space Physics*, 124(11), 9381-9404.
 896 doi: 10.1029/2019JA026590
- 897 Jonah, O. F., Coster, A., Zhang, S., Goncharenko, L., Erickson, P. J., de Paula,
 898 E. R., & Kherani, E. A. (2018, October). TID Observations and Source Anal-
 899 ysis During the 2017 Memorial Day Weekend Geomagnetic Storm Over North
 900 America. *Journal of Geophysical Research: Space Physics*, 123(10), 8749-8765.
 901 doi: 10.1029/2018JA025367
- 902 Kelley, M. C., & Fukao, S. (1991, March). Turbulent upwelling of the mid-latitude
 903 ionosphere 2. Theoretical framework. *Journal of Geophysical Research*,
 904 96(A3), 3747-3753. doi: 10.1029/90JA02252
- 905 Kelley, M. C., Vlasov, M. N., Foster, J. C., & Coster, A. J. (2004, Octo-
 906 ber). A quantitative explanation for the phenomenon known as storm-
 907 enhanced density. *Geophysical Research Letters*, 31(19), L19809. doi:
 908 10.1029/2004GL020875
- 909 Kikuchi, T., Araki, T., Maeda, H., & Maekawa, K. (1978, June). Transmission of pol-
 910 ar electric fields to the equator. *Nature*, 273, 650. doi: 10.1038/273650a0
- 911 Killeen, T. L., & Roble, R. G. (1984, September). An analysis of the high-latitude
 912 thermospheric wind pattern calculated by a Thermospheric general circula-
 913 tion model 1. Momentum forcing. *Journal of Geophysical Research*, 89(A9),
 914 7509-7522. doi: 10.1029/JA089iA09p07509
- 915 Klimenko, M. V., & Klimenko, V. V. (2012, December). Disturbance dynamo,
 916 prompt penetration electric field and overshielding in the Earth's ionosphere
 917 during geomagnetic storm. *Journal of Atmospheric and Solar-Terrestrial*
 918 *Physics*, 90, 146-155. doi: 10.1016/j.jastp.2012.02.018
- 919 Kuai, J., Liu, L., Liu, J., Sripathi, S., Zhao, B., Chen, Y., . . . Hu, L. (2016). Effects
 920 of disturbed electric fields in the low-latitude and equatorial ionosphere dur-
 921 ing the 2015 st. patrick's day storm. *Journal of Geophysical Research: Space*
 922 *Physics*, 121(9), 9111-9126. doi: 10.1002/2016JA022832

- 923 Lei, J., Huang, F., Chen, X., Zhong, J., Ren, D., Wang, W., ... Xue, X. (2018,
924 April). Was Magnetic Storm the Only Driver of the Long-Duration Enhance-
925 ments of Daytime Total Electron Content in the Asian-Australian Sector
926 Between 7 and 12 September 2017? *Journal of Geophysical Research: Space*
927 *Physics*, *123*(4), 3217-3232. doi: 10.1029/2017JA025166
- 928 Liu, L., Zou, S., Yao, Y., & Aa, E. (2019). Multi-scale ionosphere responses to the
929 May 2017 magnetic storm over the Asian sector. *GPS Solutions*, *24*, 26. doi:
930 10.1007/s10291-019-0940-1
- 931 Lu, G., Goncharenko, L., Nicolls, M. J., Maute, A., Coster, A., & Paxton, L. J.
932 (2012, August). Ionospheric and thermospheric variations associated with
933 prompt penetration electric fields. *Journal of Geophysical Research: Space*
934 *Physics*, *117*(A8), A08312. doi: 10.1029/2012JA017769
- 935 Lu, G., Goncharenko, L. P., Richmond, A. D., Roble, R. G., & Aponte, N. (2008,
936 August). A dayside ionospheric positive storm phase driven by neutral winds.
937 *Journal of Geophysical Research: Space Physics*, *113*(A8), A08304. doi:
938 10.1029/2007JA012895
- 939 Lu, G., Hagan, M. E., Häusler, K., Doornbos, E., Bruinsma, S., Anderson, B. J., &
940 Korth, H. (2014, December). Global ionospheric and thermospheric response
941 to the 5 April 2010 geomagnetic storm: An integrated data-model investiga-
942 tion. *Journal of Geophysical Research: Space Physics*, *119*(12), 10,358-10,375.
943 doi: 10.1002/2014JA020555
- 944 Lyons, L. R., Killeen, T. L., & Walterscheid, R. L. (1985, February). The neutral
945 wind “flywheel” as a source of quiet-time, polar-cap currents. *Geophysical Re-*
946 *search Letters*, *12*(2), 101-104. doi: 10.1029/GL012i002p00101
- 947 Lyons, L. R., Nishimura, Y., Gallardo-Lacourt, B., Nicolls, M. J., Chen, S., Hamp-
948 ton, D. L., ... Angelopoulos, V. (2015, June). Azimuthal flow bursts in the in-
949 ner plasma sheet and possible connection with SAPS and plasma sheet earth-
950 ward flow bursts. *Journal of Geophysical Research: Space Physics*, *120*(6),
951 5009-5021. doi: 10.1002/2015JA021023
- 952 Maruyama, N., Richmond, A. D., Fuller-Rowell, T. J., Codrescu, M. V., Sazykin, S.,
953 Toffoletto, F. R., ... Millward, G. H. (2005, September). Interaction between
954 direct penetration and disturbance dynamo electric fields in the storm-time
955 equatorial ionosphere. *Geophysical Research Letters*, *32*(17), L17105. doi:
956 10.1029/2005GL023763
- 957 McClintock, W. E., Eastes, R. W., Beland, S., Bryant, K. B., Burns, A. G., Cor-
958 reira, J., ... Veibel, V. (2020, May). Global-Scale Observations of the Limb
959 and Disk Mission Implementation: 2. Observations, Data Pipeline, and Level
960 1 Data Products. *Journal of Geophysical Research: Space Physics*, *125*(5),
961 e27809. doi: 10.1029/2020JA027809
- 962 Mendillo, M. (2006, December). Storms in the ionosphere: Patterns and processes
963 for total electron content. *Reviews of Geophysics*, *44*(4), RG4001. doi: 10
964 .1029/2005RG000193
- 965 Millward, G. H., Moffett, R. J., Balmforth, H. F., & Rodger, A. S. (1999, Novem-
966 ber). Modeling the ionospheric effects of ion and electron precipitation in the
967 cusp. *Journal of Geophysical Research: Space Physics*, *104*(A11), 24603-24612.
968 doi: 10.1029/1999JA900249
- 969 Nava, B., Rodríguez-Zuluaga, J., Alazo-Cuartas, K., Kashcheyev, A., Migoya-
970 Orué, Y., Radicella, S. M., ... Fleury, R. (2016, April). Middle- and low-
971 latitude ionosphere response to 2015 St. Patrick’s Day geomagnetic storm.
972 *Journal of Geophysical Research: Space Physics*, *121*(4), 3421-3438. doi:
973 10.1002/2015JA022299
- 974 Ngwira, C. M., McKinnell, L.-A., Cilliers, P. J., & Coster, A. J. (2012, January).
975 Ionospheric observations during the geomagnetic storm events on 24-27 July
976 2004: Long-duration positive storm effects. *Journal of Geophysical Research:*
977 *Space Physics*, *117*, A00L02. doi: 10.1029/2011JA016990

- 978 Perkins, F. (1973). Spread F and ionospheric currents. *J. Geophys. Res.*, *78*, 218-
979 226. doi: 10.1029/JA078i001p00218
- 980 Pröls, G. W. (1976, June). On explaining the negative phase of ionospheric storms.
981 *Planetary and Space Science*, *24*(6), 607-609. doi: 10.1016/0032-0633(76)90140
982 -9
- 983 Pröls, G. W. (2008, January). Ionospheric storms at mid-latitude: A short review.
984 *Washington DC American Geophysical Union Geophysical Monograph Series*,
985 *181*, 9-24. doi: 10.1029/181GM03
- 986 Raeder, J., Cramer, W. D., Jensen, J., Fuller-Rowell, T., Maruyama, N., Toffo-
987 letto, F., & Vo, H. (2016, November). Sub-Auroral Polarization Streams:
988 A complex interaction between the magnetosphere, ionosphere, and thermo-
989 sphere. In *Journal of physics conference series* (Vol. 767, p. 012021). doi:
990 10.1088/1742-6596/767/1/012021
- 991 Richmond, A. D. (1978, September). Gravity wave generation, propagation, and dis-
992 sipation in the thermosphere. *Journal of Geophysical Research: Space Physics*,
993 *83*(A9), 4131-4146. doi: 10.1029/JA083iA09p04131
- 994 Richmond, A. D., & Lu, G. (2000, August). Upper-atmospheric effects of magnetic
995 storms: a brief tutorial. *Journal of Atmospheric and Solar-Terrestrial Physics*,
996 *62*(12), 1115-1127. doi: 10.1016/S1364-6826(00)00094-8
- 997 Rideout, W., & Coster, A. (2006). Automated gps processing for global total elec-
998 tron content data. *GPS Solut.*, *10*(3), 219-228. doi: 10.1007/s10291-006-0029
999 -5
- 1000 Rishbeth, H. (1979, August). Ion-drag effects in the thermosphere. *Journal of Atmo-*
1001 *spheric and Terrestrial Physics*, *41*, 885-894. doi: 10.1016/0021-9169(79)90130
1002 -2
- 1003 Rishbeth, H. (1998, September). How the thermospheric circulation affects the
1004 ionospheric F2-layer. *Journal of Atmospheric and Solar-Terrestrial Physics*,
1005 *60*(14), 1385-1402. doi: 10.1016/S1364-6826(98)00062-5
- 1006 Rodger, A. (2008, January). The mid-latitude trough—Revisited. *Washington DC*
1007 *American Geophysical Union Geophysical Monograph Series*, *181*, 25-33. doi:
1008 10.1029/181GM04
- 1009 Savitzky, A., & Golay, M. J. E. (1964, January). Smoothing and differentiation
1010 of data by simplified least squares procedures. *Analytical Chemistry*, *36*, 1627-
1011 1639.
- 1012 Schunk, R. W. (1975, March). Transport equations for aeronomy. *Planetary and*
1013 *Space Science*, *23*(3), 437-485. doi: 10.1016/0032-0633(75)90118-X
- 1014 Schunk, R. W., & Nagy, A. F. (2000). *Ionospheres: physics, plasma physics, and*
1015 *chemistry*. Cambridge University Press.
- 1016 Semeter, J., Butler, T., Heinselman, C., Nicolls, M., Kelly, J., & Hampton, D. (2009,
1017 May). Volumetric imaging of the auroral ionosphere: Initial results from
1018 PFISR. *Journal of Atmospheric and Solar-Terrestrial Physics*, *71*(6-7), 738-
1019 743. doi: 10.1016/j.jastp.2008.08.014
- 1020 Shiokawa, K., Otsuka, Y., Ogawa, T., Balan, N., Igarashi, K., Ridley, A. J., . . . Yu-
1021 moto, K. (2002, June). A large-scale traveling ionospheric disturbance during
1022 the magnetic storm of 15 September 1999. *Journal of Geophysical Research:*
1023 *Space Physics*, *107*(A6), 1088. doi: 10.1029/2001JA000245
- 1024 Shiokawa, K., Otsuka, Y., Ogawa, T., Kawamura, S., Yamamoto, M., Fukao, S., . . .
1025 Yumoto, K. (2003, December). Thermospheric wind during a storm-time large-
1026 scale traveling ionospheric disturbance. *Journal of Geophysical Research: Space*
1027 *Physics*, *108*(A12), 1423. doi: 10.1029/2003JA010001
- 1028 Singh, R., & Sripathi, S. (2017, November). Ionospheric Response to 22-23 June
1029 2015 Storm as Investigated Using Ground-Based Ionosondes and GPS Re-
1030 ceivers Over India. *Journal of Geophysical Research: Space Physics*, *122*(11),
1031 11,645-11,664. doi: 10.1002/2017JA024460
- 1032 Spiro, R. W., Heelis, R. A., & Hanson, W. B. (1979, Aug). Rapid subauroral ion

- 1033 drifts observed by Atmosphere Explorer C. *Geophysical Research Letters*, 6(8),
 1034 657-660. doi: 10.1029/GL006i008p00657
- 1035 Su, Y. J., Caton, R. G., Horwitz, J. L., & Richards, P. G. (1999, January). Sys-
 1036 tematic modeling of soft-electron precipitation effects on high-latitude F region
 1037 and topside ionospheric upflows. *Journal of Geophysical Research: Space*
 1038 *Physics*, 104(A1), 153-164. doi: 10.1029/1998JA900068
- 1039 Tsurutani, B., Mannucci, A., Iijima, B., Abdu, M. A., Sobral, J. H. A., Gon-
 1040 zalez, W., ... Vasyliunas, V. M. (2004, August). Global dayside iono-
 1041 spheric uplift and enhancement associated with interplanetary electric fields.
 1042 *Journal of Geophysical Research: Space Physics*, 109(A8), A08302. doi:
 1043 10.1029/2003JA010342
- 1044 Varney, R. H., Nicolls, M. J., Heinselman, C. J., & Kelley, M. C. (2009, March).
 1045 Observations of polar mesospheric summer echoes using PFISR during the
 1046 summer of 2007. *Journal of Atmospheric and Solar-Terrestrial Physics*, 71(3-
 1047 4), 470-476. doi: 10.1016/j.jastp.2009.01.002
- 1048 Vierinen, J., Coster, A. J., Rideout, W. C., Erickson, P. J., & Norberg, J. (2016).
 1049 Statistical framework for estimating GNSS bias. *Atmospheric Measurement*
 1050 *Techniques*, 9, 1303-1312. doi: 10.5194/amt-9-1303-2016
- 1051 Wang, H., Lühr, H., HäUslér, K., & Ritter, P. (2011, March). Effect of sub-
 1052 auroral polarization streams on the thermosphere: A statistical study.
 1053 *Journal of Geophysical Research: Space Physics*, 116(A3), A03312. doi:
 1054 10.1029/2010JA016236
- 1055 Wang, H., Zhang, K., Zheng, Z., & Ridley, A. J. (2018, March). The effect of sub-
 1056 auroral polarization streams on the mid-latitude thermospheric disturbance
 1057 neutral winds: a universal time effect. *Annales Geophysicae*, 36(2), 509-525.
 1058 doi: 10.5194/angeo-36-509-2018
- 1059 Wang, W., Talaat, E. R., Burns, A. G., Emery, B., Hsieh, S.-y., Lei, J., & Xu, J.
 1060 (2012, July). Thermosphere and ionosphere response to subauroral polarization
 1061 streams (SAPS): Model simulations. *Journal of Geophysical Research: Space*
 1062 *Physics*, 117(A7), A07301. doi: 10.1029/2012JA017656
- 1063 Watari, S. (2017, May). Geomagnetic storms of cycle 24 and their solar sources.
 1064 *Earth, Planets, and Space*, 69(1), 70. doi: 10.1186/s40623-017-0653-z
- 1065 Yeh, H. C., & Foster, J. C. (1990, June). Storm tide heavy ion outflow at mid-
 1066 latitude. *Journal of Geophysical Research: Space Physics*, 95(A6), 7881-7891.
 1067 doi: 10.1029/JA095iA06p07881
- 1068 Yue, X., Wang, W., Lei, J., Burns, A., Zhang, Y., Wan, W., ... Schreiner, W. S.
 1069 (2016, September). Long-lasting negative ionospheric storm effects in low and
 1070 middle latitudes during the recovery phase of the 17 March 2013 geomagnetic
 1071 storm. *Journal of Geophysical Research: Space Physics*, 121(9), 9234-9249.
 1072 doi: 10.1002/2016JA022984
- 1073 Zakharenkova, I., Astafyeva, E., & Cherniak, I. (2016, December). GPS and
 1074 GLONASS observations of large-scale traveling ionospheric disturbances during
 1075 the 2015 St. Patrick's Day storm. *Journal of Geophysical Research: Space*
 1076 *Physics*, 121(12), 12,138-12,156. doi: 10.1002/2016JA023332
- 1077 Zhang, S.-R., Erickson, P. J., Coster, A. J., Rideout, W., Vierinen, J., Jonah, O., &
 1078 Goncharenko, L. P. (2019, December). Subauroral and Polar Traveling Iono-
 1079 spheric Disturbances During the 7-9 September 2017 Storms. *Space Weather*,
 1080 17(12), 1748-1764. doi: 10.1029/2019SW002325
- 1081 Zhang, S.-R., Erickson, P. J., Foster, J. C., Holt, J. M., Coster, A. J., Makela, J. J.,
 1082 ... Kerr, R. B. (2015, July). Thermospheric poleward wind surge at mid-
 1083 latitudes during great storm intervals. *Geophysical Research Letters*, 42(13),
 1084 5132-5140. doi: 10.1002/2015GL064836
- 1085 Zhang, S.-R., Erickson, P. J., Zhang, Y., Wang, W., Huang, C., Coster, A. J., ...
 1086 Kerr, R. (2017, January). Observations of ion-neutral coupling associated
 1087 with strong electrodynamic disturbances during the 2015 St. Patrick's Day

- 1088 storm. *Journal of Geophysical Research: Space Physics*, 122(1), 1314-1337.
1089 doi: 10.1002/2016JA023307
- 1090 Zhang, S.-R., Zhang, Y., Wang, W., & Verkhoglyadova, O. P. (2017, June).
1091 Geospace system responses to the St. Patrick's Day storms in 2013 and 2015.
1092 *Journal of Geophysical Research: Space Physics*, 122(6), 6901-6906. doi:
1093 10.1002/2017JA024232
- 1094 Zhong, J., Wang, W., Yue, X., Burns, A. G., Dou, X., & Lei, J. (2016). Long-
1095 duration depletion in the topside ionospheric total electron content during
1096 the recovery phase of the march 2015 strong storm. *Journal of Geophysical*
1097 *Research: Space Physics*, 121(5), 4733-4747. doi: 10.1002/2016JA022469
- 1098 Zou, S., Moldwin, M. B., Ridley, A. J., Nicolls, M. J., Coster, A. J., Thomas, E. G.,
1099 & Ruohoniemi, J. M. (2014, October). On the generation/decay of the storm-
1100 enhanced density plumes: Role of the convection flow and field-aligned ion
1101 flow. *Journal of Geophysical Research: Space Physics*, 119(10), 8543-8559. doi:
1102 10.1002/2014JA020408
- 1103 Zou, S., Ridley, A., Jia, X., Boyd, E., Nicolls, M., Coster, A., ... Ruohoniemi, J. M.
1104 (2017, February). PFISR observation of intense ion upflow fluxes associated
1105 with an SED during the 1 June 2013 geomagnetic storm. *Journal of Geophysi-*
1106 *cal Research: Space Physics*, 122(2), 2589-2604. doi: 10.1002/2016JA023697
- 1107 Zou, S., Ridley, A. J., Moldwin, M. B., Nicolls, M. J., Coster, A. J., Thomas, E. G.,
1108 & Ruohoniemi, J. M. (2013, December). Multi-instrument observations of SED
1109 during 24-25 October 2011 storm: Implications for SED formation processes.
1110 *Journal of Geophysical Research: Space Physics*, 118(12), 7798-7809. doi:
1111 10.1002/2013JA018860